

Identifying parent bodies of meteorites among near-Earth asteroids

A. Carbognani^{1*} and M. Fenucci^{2,3}

¹INAF - Osservatorio di Astrofisica e Scienza dello Spazio, Via Gobetti 93/3, 40129 Bologna, Italy

²ESA ESRIIN / PDO / NEO Coordination Centre, Largo Galileo Galilei, 1, 00044 Frascati (RM), Italy

³Elecnor Deimos, Via Giuseppe Verdi, 6, 28060 San Pietro Mosezzo (NO), Italy

Accepted XXX. Received YYY; in original form ZZZ

ABSTRACT

Meteorites provide an important source of information about the formation and composition of asteroids, because the level of accuracy of studies and analyses performed in a laboratory cannot be achieved by any ground or space based observation. To better understand what asteroid types a meteorite represents, it is crucial to identify the body they originated from. In this paper, we aim to determine possible parent bodies for the known meteorite falls among the known population of near-Earth asteroids (NEAs). By using the similarity criterion D_N , based on geocentric quantities, we found 20 possible NEA-meteorite pairs. By performing additional numerical simulations of the backward dynamics, we found that 12 of these pairs may be associated with a possible separation event from the progenitor NEA, while the remaining 8 pairs appear to be ambiguous or random associations. The most interesting are the Pribram and Neuschwanstein meteorites, which are dynamically associated with (482488) 2012 SW20 with a common separation age dating back to about 20–30 kyr ago, and the Motopi Pan meteorite, that has three candidate parent bodies: (454100) 2013 BO73, 2017 MC3, and 2009 FZ4. The average time of separation between our meteorite list and the progenitor body appears to be about 10 kyr, a time consistent with what is expected from the collision frequency of small NEAs. Based on our results, we suggest that about 25 per cent of meteorites do not originate in the main belt, but mainly from little collision events happening between NEAs in the inner Solar System.

Key words: meteorites, meteors, meteoroids – minor planets, asteroids: general – celestial mechanics

1 INTRODUCTION

The Earth’s atmosphere is continuously bombarded by small near-Earth-type asteroids. According to NASA’s CNEOS data center¹, there is an event detectable by military satellites on average every two weeks, with a mean diameter of about 1-2 m. About 9.8% of the events belong to Jupiter Family Comets, while 85.5% have a Tisserand parameter with respect to Jupiter typical of asteroid orbits (Peña-Asensio, Trigo-Rodríguez & Rimola 2022).

These meteoroids enter the atmosphere at speeds of several tens of km per second, give rise to brilliant fireballs, and disintegrate as they fall into the deep atmosphere due to the compression exerted on meteoroid by the shock wave. The first disintegration occurs at variable altitudes according to the strength of the body (0.1–4 MPa), while the extinction occurs at altitudes of some tens of km (Borovička et al. 2008). For fireballs arriving at lower altitudes, between 20 and 30 km in height, there is a good chance that the fragments of the original meteoroid begin the dark flight phase and give rise to the recovery of meteorites on the ground.

From the heliocentric orbits of the meteoroids associated with meteorites, we know that they originate from the asteroids population, but it is difficult to identify which are the progenitors. Notable exceptions are the asteroid Vesta and meteorites of the HED (Howardite–Eucrite–Diogenite) type. In this case the association

was facilitated by the optical reflectance spectral features similar to those of Vesta and other smaller asteroids belonging to the Vesta family (Binzel & Xu 1993). In general, the problem is not so easy. For example, the progenitor bodies of the ordinary chondrites (OC) which make up about 80% of the falls are S-type asteroids, but they are not yet identified with certainty. OCs must have originated from at least three progenitor bodies, so as to explain the presence of chondrites of type H (42.5% of the OCs), L (46.2%) and LL (11.3%) according to the decreasing content of iron and metals (Vernazza et al. 2015).

According to the current paradigm, the progenitor meteoroids of meteorites were formed millions of years ago following collisions between main-belt asteroids that created asteroid families. Subsequently, due to the mean-motion orbital resonances with Jupiter and the Yarkovsky effect, they were placed on near-Earth type orbits which led them to fall on Earth (see e.g. Bottke et al. 2002; Granvik et al. 2017, 2018, and references therein). For example, this would be the origin of some L chondrites (Creston, Novato, Innisfree, and Jesenice) and the rare EL enstatite chondrite associated to main belt asteroid (161) Athor (Jenniskens et al. 2019; Avdellidou et al. 2022). The prominent Flora family in the inner part of the main belt is a good candidate to be the origin of rare LL-type ordinary chondrites (Vernazza et al. 2008), while the large S-type asteroid (6) Hebe, located adjacent to both the ν_6 secular resonance with Saturn and 3:1 mean-motion resonance with Jupiter is the probable source of H-type OC (Morbidelli et al. 1994; Gaffey & Gilbert 1998). Also Granvik & Brown (2018), recalculating the orbits of 25

* E-mail: -

¹ <https://cneos.jpl.nasa.gov/>

known meteorite falls based on the trajectory information reported in the literature, finds that most meteorite originate in the inner main asteroid belt and escape through the 3:1 mean-motion resonance or the ν_6 secular resonance.

However, it cannot be excluded that a part of the meteorites also originates directly from the dynamic population of the near-Earth asteroids (NEAs). Possible formation mechanisms include collisions with smaller NEAs, thermal fragmentation (Delbo et al. 2014; Granvik et al. 2016), partial rotational disaggregation of rubble piles due to YORP effect (Scheeres 2018), tidal disruption of rubble piles during flyby with planets (Zhang & Michel 2020), sublimation of small reserves of volatile materials, or as a result of activity mechanisms not yet well understood on the asteroid's surface as for (3200) Phaethon, the progenitor of the Geminid meteoroid stream (Whipple 1983; Williams & Wu 1993), and (101955) Bennu (Melikyan et al. 2021). In the case of this last NEA, the activity of ejecting stones into space is detectable only from spacecraft, but not through observations from the ground because the intensity is too low.

The rotational disaggregation due to YORP effect appears to be the primary formation processes for small close binaries between the population of NEAs: the estimated proportion of binaries among NEAs larger than 0.3 km is $15 \pm 4\%$ (Pravec et al. 2006). Pairs of asteroids share similar heliocentric orbits but they are not bound together: integrations of their orbits indicated that they separated with low relative velocities, so they can be considered as unborn binaries with the same physical formation processes (Pravec et al. 2010). Most of the known pairs are found between main-belt asteroids (Kyrylenko, Krugly & Golubov 2021), but at least two pairs of asteroids (2015 EE7–2015 FP124 and 2017 SN16–2018 RY7), have also been identified in the NEAs population, suggesting a common origin and a very recent separation between the two components, estimated in about 10 kyr for the second pair (Moskovitz et al. 2019). In both cases – binary or pairs – it is possible to have the dispersion, on the original orbit, of large meteoroids capable of generating fireballs and meteorites. All the physical processes mentioned above fall in the heterogeneous category of active asteroids, transversal to both main belts and NEAs (Jewitt 2012); for a recent review about meteor showers from active asteroids and dormant comets between NEAs see Quan-Zhi Ye (2018).

One objection to this hypothesis of connection between NEAs and meteorites may be that NEAs cannot be progenitors of meteoroids producing meteorites because about 2/3 of the NEAs have spectra compatible with ordinary LL-type chondrites which are a minority compared to other types of meteorites (Vernazza et al. 2015). While this may be true in a statistical sense, it does not rule out the possibility that there are some NEAs that, by means of some of the physical processes mentioned above, can release large meteoroids into interplanetary space forming faint meteoroids stream along the orbit. Furthermore, considering that the NEA population contains asteroids that pose a risk to the Earth and that the mitigation strategy depends on the composition of the object, try associating meteorites and NEAs can be a good way to get low-cost information on potentially dangerous asteroids and the meteorite-NEAs association may become very important also in view of the mining of asteroids because it is possible to have useful information to decide which asteroids to exploit (O'Leary 1977). Recently, a dynamical association between the impactor 2018LA and the Potentially Hazardous Asteroid (454100) 2013 BO73 have been proposed (de la Fuente Marcos & de la Fuente Marcos 2019) and, as we see later, we find the same association.

So the question we want to answer is: are there NEAs that could

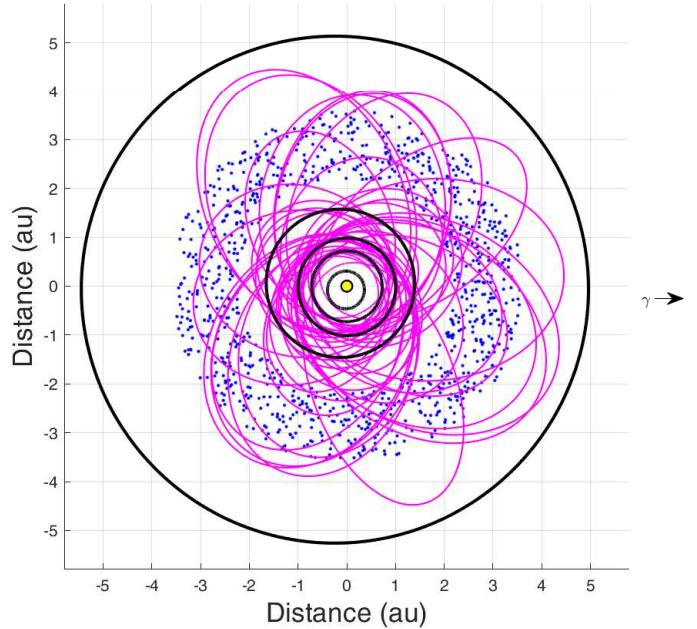


Figure 1. The meteorites orbits of Table 1 projected on the ecliptic plane. The outer circle is the Jupiter's orbit. The main belt is represented by dots with a random distribution.

be the progenitors - or brothers - of some of the meteorites known today? To answer this question, we investigated the possible orbital connection between meteorites and NEAs in order to identify those that are the most probable progenitors of meteorites whose heliocentric orbit is known. For this reason, only the meteorites whose fireball was directly triangulated during the atmospheric fall were taken into consideration, see Table 1 for a list and Figure 1 for heliocentric orbits plot.

The paper is organized as follow: in Section 2 we will see the adopted criterion for orbits similarity. In Section 3 we will see the list of the most probable associations between meteorites and NEAs, while in Section 4 we will see the results about the numerical integration of the orbits to dynamically establish the connection between NEAs and meteorites. In Section 5 we discuss the results obtained and finally we provide our conclusions.

2 ADOPTED CRITERION FOR ORBITS SIMILARITY

In general, the Southworth & Hawkins (1963) Dissimilarity Criterion D or its variants (see e.g. Drummond 1981; Jopek 1993; Jenniskens 2008; Rožek, Breiter & Jopek 2011), is used to search for a connection between the observed orbits of the meteors and the progenitor body. Usually a value $D \leq 0.1$ indicates a higher degree of similarity between two orbits. A first problem with this approach is that the meteor's heliocentric orbital elements are derived quantities and cannot always be determined with precision comparable to that of asteroids. A second problem is that orbits change over time due to planetary perturbations, so the value of D may not be indicative of a common origin (Quan-Zhi Ye 2018). In the case of meteors and fireballs it is therefore more convenient to use the similarity criterion D_N , based on geocentric quantities, introduced

Table 1. List of meteorites with a heliocentric orbit from fireballs triangulation sorted by date of fall in Julian Days (JD): a = semi major axis; e = eccentricity; i = orbit inclination; Ω = longitude of ascending node; ω = argument of perihelion; M = mean anomaly of the fall. Orbital elements for equinox J2000.0. Meteorite type: OC = ordinary chondrite; C = carbonaceous chondrite; EC= enstatite chondrite; AE= achondrite Eucrite; AH=achondrite Howardite; U=Ureilite. In this table meteorites type are from Meteoritical Bulletin Database (<https://www.lpi.usra.edu/meteor/>). For an extensive set of references regarding this list of meteorites you can consult the Meteorite Orbits.info website (<https://www.meteoriteorbits.info/>). These databases were last consulted on May 10, 2023.

N	Name	Type	a (au)	e	i (°)	Ω (°)	ω (°)	M (°)	JD fall
01	Pribram	OC H5	2.40±0.002	0.6711±0.0003	10.482±0.0004	17.79147±0.00001	241.75±0.013	349.539	2436666.333
02	Lost City	OC H5	1.66±0.05	0.417±0.005	12.0±0.5	283.0±0.5	161.0±0.5	7.182	2440591.333
03	Innisfree	OC L5	1.87±0.005	0.4732±0.0005	12.27±0.05	316.80±0.05	177.97±0.05	0.640	2443181.292
04	Benesov	OC LL3.5	2.48±0.002	0.6274±0.0004	23.981±0.007	47.0009±0.0001	218.370±0.008	352.417	2448384.458
05	Peekskill	OC H6	1.49±0.03	0.41±0.01	4.9±0.2	17.030±0.001	308.0±1.0	21.540	2448905.292
06	Tagish Lake	C2-ung	2.1±0.2	0.57±0.05	1.4±0.9	297.900±0.003	222.0±2.0	349.895	2451561.833
07	Moravka	OC H5	1.85±0.07	0.47±0.02	32.2±0.5	46.2580±0.00005	203.5±0.6	352.385	2451671.042
08	Neuschwanstein	EC EL6	2.40±0.02	0.670±0.002	11.41±0.03	16.82664±0.00001	241.20±0.06	349.420	2452371.347
09	Park Forest	OC L5	2.53±0.19	0.680±0.023	3.2±0.3	6.1156±0.0007	237.5±1.6	350.715	2452725.493
10	Villalbedo de la Peña	OC L6	2.3±0.2	0.63±0.04	0.0±0.2	283.6712±0.00005	132.3±1.5	9.229	2453009.199
11	Bunburra Rockhole	AE	0.85±0.0004	0.2427±0.0005	8.95±0.03	297.595±0.0005	210.04±0.06	133.571	2454302.301
12	Almahata Sitta	U	1.308201±0	0.31206±0	2.54220±0	194.101138±0	234.44897±0	330.834	2454746.615
13	Buzzard Coulee	OC H4	1.25±0.02	0.23±0.02	25.0±0.8	238.93739±0.00008	211.3±1.4	340.573	2454791.518
14	Maribo	CM2	2.43± 0.2	0.805±0.011	0.25±0.16	297.46±0.15	279.4±0.6	348.713	2454849.299
15	Jesenice	OC L6	1.75±0.07	0.431±0.022	9.6±0.5	019.196±0.0005	190.5±0.5	356.220	2454930.583
16	Grimsby	OC H5	2.04± 0.05	0.518±0.011	28.07±0.28	182.9561±0.00005	159.865±0.43	5.548	2455100.544
17	Košice	OC H5	2.71±0.24	0.647±0.032	2.0±0.8	340.072±0.004	204.2±1.2	355.951	2455256.434
18	Mason Gully	OC H5	2.470±0.004	0.6023±0.009	0.832±0.013	203.2112±0.00005	218.95±0.03	351.810	2455299.941
19	Križevci	OC H6	1.544±0.01	0.521±0.004	0.64±0.03	315.55±0.01	254.4±0.1	335.381	2455597.472
20	Sutter's Mill	C	2.59±0.35	0.824±0.02	2.38±1.16	32.77±0.06	77.8±3.2	10.452	2456040.118
21	Novato	OC L6	2.088±0.077	0.526±0.017	5.508±0.040	24.99±0.0035	347.352±0.134	3.360	2456218.613
22	Chelyabinsk	OC LL5	1.72±0.02	0.571±0.006	4.98±0.12	326.459±0.001	107.67±0.17	20.000	2456338.640
23	Annama	OC H5	1.99±0.12	0.69 ±0.02	14.65±0.46	28.611±0.001	264.77±0.55	344.111	2456766.426
24	Žd'ár nad Sázavou	OC L3	2.093±0.006	0.6792±0.001	2.796±0.009	257.262±0.010	257.721±0.014	345.583	2457001.178
25	Porangaba	OC L4	2.45±1.10	0.64±0.11	8.6±3.2	288.921±0.001	142.8±6.7	6.638	2457032.232
26	Sarıççek	AH	1.454±0.083	0.304±0.039	22.6±1.6	159.849±0.004	182.8±1.6	358.576	2457268.342
27	Creston	OC L6	1.300±0.019	0.410±0.013	4.228±0.070	30.458±0.006	7.20±0.13	323.239	2457319.741
28	Murrilli	OC H5	2.521±0.075	0.609±0.012	3.32±0.060	64.742±0.0033	354.557±0.039	1.050	2457353.947
29	Ejby	OC H5/6	2.81±0.09	0.65±0.011	0.96±0.10	317.211±0.0001	197.75±0.10	357.102	2457425.380
30	Stubenberg	OC LL6	1.525±0.010	0.395±0.004	2.07±0.03	346.520±0.0001	221.02±0.03	342.834	2457454.400
31	Dishchii' bikoh	OC LL7	1.129±0.008	0.205±0.004	21.24±0.27	72.1206±0.0002	108.7±1.5	50.231	2457541.955
32	Dingle Dell	OC LL6	2.254±0.034	0.5905±0.0063	4.051±0.012	218.252±0.00032	215.773±0.049	352.191	2457693.002
33	Hamburg	OC H4	2.73±0.05	0.661±0.006	0.604±0.11	296.421±0.03	211.65±0.3	354.949	2458135.547
34	Motopi Pan	AH	1.3764±0.0001	0.43186±0.00006	4.2974±0.0004	71.869605±0.000012	256.04869±0.00055	327.170	2458272.197
35	Ozerki	OC L6	0.84±0.02	0.199±0.03	18.443±3.047	89.656± ?	335.286±5.147	215.712	2458290.553
36	Viñales	OC L6	1.217±0.005	0.391±0.005	11.47±0.05	132.28 ±0.005	276.97±0.05	306.489	2458516.262
37	Arpu Kuilpu	OC H5	2.75±0.03	0.671±0.003	2.03±0.01	250.36±0.01	43.25±0.02	353.166	2458635.912
38	Flensburg	C1	2.82±0.03	0.701±0.003	6.82±0.06	349.207±0.001	307.25±0.16	7.480	2458739.035
39	Cavezzo	OC L5-an	1.82±0.22	0.46±0.063	4.0±1.6	280.52311±0.00001	179.2±4.8	0.261	2458850.268
40	Novo Mesto	OC L5	1.451±0.004	0.6086±0.0006	8.755±0.063	338.993041±0.00001	82.649±0.184	28.826	2458907.896
41	Madura Cave	OC L5	0.889±0.003	0.327±0.009	0.12±0.08	88.703764±0.00001	312.02±0.51	260.842	2459020.336
42	Traspena	OC L5	1.125±0.016	0.386±0.013	4.55±0.19	297.8270±0.0003	273.93±0.98	309.939	2459232.514
43	Winchcombe	CM2	2.5855±0.0077	0.6183±0.0011	0.460±0.014	160.1955±0.0014	351.798±0.018	1.524	2459274.410
44	Antonin	OC L5	1.1269±0.0007	0.2285±0.0006	24.22±0.05	112.5807±0.0001	257.16±0.09	307.227	2459410.625

by Valsecchi, Jopek & Froeschlé (1999) for the identification of new meteor showers. The D_N function is defined as follows:

$$D_N^2 = [U_2 - U_1]^2 + [\cos \theta_1 - \cos \theta_2]^2 + \Delta\xi^2, \quad (1)$$

where

$$\Delta\xi^2 = \min(\Delta\phi_I^2 + \Delta\lambda_I^2, \Delta\phi_{II}^2 + \Delta\lambda_{II}^2) \quad (2)$$

$$\Delta\phi_I = 2 \sin\left(\frac{\phi_1 - \phi_2}{2}\right) \quad (3)$$

$$\Delta\phi_{II} = 2 \sin\left(\frac{180^\circ + \phi_2 - \phi_1}{2}\right) \quad (4)$$

$$\Delta\lambda_I = 2 \sin\left(\frac{\lambda_1 - \lambda_2}{2}\right) \quad (5)$$

$$\Delta\lambda_{II} = 2 \sin\left(\frac{180^\circ + \lambda_2 - \lambda_1}{2}\right). \quad (6)$$

where xyz is a Cartesian coordinate system centered on the Earth

with the y axis facing the direction of the Earth's motion, the x axis opposite to the direction of the Sun and the z axis orthogonal to the ecliptic plane, D_N depends on 4 geocentric quantities directly related to the observations: U , the normalized geocentric speed of the body in units of the mean speed of the Earth (29.7 km s^{-1}); θ , the angle between the direction of motion of the Earth along the y axis and the U vector; ϕ , the angle between the U vector and the xz plane, and finally λ , the heliocentric longitude of the Earth at the encounter with the meteor shower. The angles θ and ϕ are directly related to the radiant, a quantity that for meteors and fireballs is directly observable and U is a different way of considering the geocentric velocity of the meteoroid. Moreover, D_N also has the advantage of being partially invariant under secular perturbations. The invariant quantities are U and $\cos \theta$: the first because it depends only from the Tisserand invariant with respect to the Earth, the second because it depends from U and $1/a$ which is a constant due to the conservation of orbital energy (Valsecchi, Jopek & Froeschlé 1999). For the computation of D_N it is assumed that the orbit of the Earth is circular with a radius equal to 1 au. In reality the orbit is slightly elliptical and this involves an error on θ and ϕ of the order of one degree, a negligible amount because the values of the cosine and sine functions change little. For NEAs whose orbit intersects that of the Earth, the quantities U , θ , ϕ and λ that define the type of geocentric encounter can be computed once the heliocentric osculating orbital elements are known (Valsecchi, Jopek & Froeschlé 1999). In the case of meteors or fireballs, the quantities U , θ and ϕ or the equivalent $\vec{U} = U_x \hat{x} + U_y \hat{y} + U_z \hat{z}$ come from the geocentric position of the true radiant and the geocentric velocity according to the following formula (Valsecchi, Jopek & Froeschlé 1999)²:

$$\vec{U} = \hat{\mathbf{r}}(-\lambda)\hat{\mathbf{p}}(-\epsilon)\frac{V_G}{29.7}\begin{pmatrix} -\cos \delta_G \cos \alpha_G \\ -\cos \delta_G \sin \alpha_G \\ -\sin \delta_G \end{pmatrix}. \quad (7)$$

In Eq. (7) $\hat{\mathbf{r}}(-\lambda)$ and $\hat{\mathbf{p}}(-\epsilon)$ are rotation matrices around z -axes and x -axes respectively, λ is the ecliptic longitude of the Earth and ϵ is the inclination of the ecliptic above equatorial plane. The position of the true geocentric radiant α_G and δ_G is measured directly from the trajectory of the fireball, while to get the geocentric speed V_G it is enough to correct the entry speed into the atmosphere for the gravitational attraction of the Earth: these are quantities directly correlated to the observables of the fireball. Unfortunately not all the papers relating to fireballs of which meteorites have been recovered and orbit computed have these data³. We recommend that fireballs observers always include the true geocentric radiant and the geocentric velocity in their tables. Table A1, computed from Eq. (7) with $\theta = \arccos(U_y/U)$ and $\phi = \arctan(U_x/U_z)$, shows U , θ , ϕ and λ values for the meteorites listed in Table 1, excluding those for which information on true radian and geocentric velocity has not been found.

Figure 2 shows the distribution of the true geocentric radiants of the meteorites listed in Table A1 and those of NEAs that intersect the Earth's orbit. As we can see the meteorites Innisfree (3), Sariçiçek (22), Murrili (24), Ejby (25) and Cavezzo (33), are in areas where the density of NEAs is low and the association with a possible near-Earth is statistically simpler.

² There was a typo in Valsecchi, Jopek & Froeschlé (1999), the rotations are $-\lambda$ and $-\epsilon$.

³ Missing data for Almahata Sitta, Bouzzard Coulee, Mason Gully, Stubenberg, Tagish Lake and Viñales.

2.1 The limit value for D_N

It is well known that the orbits of planet-crossing objects, including both NEAs and comets, are very chaotic so the orbital elements of NEAs evolve quickly due to the effect of planetary perturbations (Gronchi & Michel 2001). In general, for the orbits of NEAs the most important gravitational perturbations can be secular, i.e. independent from the mean longitude on the orbit, resonant i.e. dependent by the semi-major axis of the orbit, or of short period if they cannot be classified in the first two types. Secular perturbations act on time scales of thousands of years and can be seen in the values of the argument of perihelion ω and of the ascending node Ω which can grow or decrease linearly over time through all the values between 0° and 360° and in those of the eccentricity and inclination which instead oscillates. On the other hand, the semi-major axis is invariant under secular perturbations. For a generic NEA that is not in resonance conditions, the most important perturbations to describe its long term orbital evolution are the secular ones.

For a typical NEA the secular ω cycle usually lasts from 5 000 to 10 000 years. For each ω cycle a NEA's orbit can intersect the Earth's orbit four times so they are called quadruple Earth crossers, but also octuple crossers are possible. Statistically, Earth-crossers are more probable in Apollo and Aten classes, defined on the basis of the current osculating elements, but Apollo and Aten are not equivalent to the class of Earth-crossing asteroids. Amor-type asteroids do not intersect the Earth's orbit, but a NEA can also switch from one orbital class to another with times of the order of thousands of years due to secular perturbations (Gronchi & Milani 2001). Considering that, for a given NEA, we do not know when the separation between the progenitor body and the meteoroid producing the meteorite took place, we must consider all the intersections that can occur with the Earth's orbit for one entire variation of ω . In this way a connection can also be found between a meteorite and a NEA which are in a different phase of their ω cycle. For the secular evolution of NEAs we adopted the integration method by Gronchi & Milani (2001), that allows to compute the secular evolution of the elements e , i , Ω and ω and to get all the crossing conditions.

The list of NEAs geocentric encounter conditions U , θ , ϕ and λ maintained by NEODYS-2 was used⁴. This list was computed with the OrbFit software⁵ that gives the encounter conditions for 16 227 NEAs of the total 30 740 actual population which, during their ω cycle, intersect Earth's orbit. This is a crucial point and it should be emphasized: the computation of the encounters conditions for asteroids whose orbit is not crossing the Earth at the present time, but can cross at some time in the future and in the past, can be used in the search for parent bodies of meteor streams or fireballs (Gronchi & Milani 2001). A similar strategy can also be found in Babadzhanov, Williams & Kokhirova (2012), who computes the geocentric radiants of the orbits of NEAs crossing Earth's orbit on a ω cycle and compares them with those of observed meteor showers searching for dormant comets among the NEAs. As stated above a NEA can be a quadruple or octuple crossers, depending on the number of possible intersections with the Earth's orbit during the ω cycle. The intersection can take place at the ascending or descending node and - fixed the node - can be pre or post perihelion.

Once you have a criterion definition, it is also necessary to establish the maximum D_N value ($D_{N_{\max}}$), beyond which the association between meteorites and NEAs begins to lose meaning due to the oc-

⁴ <https://newton.spacedys.com/~neody2/propneo/encounter.cond>
This list were last consulted on Nov 18, 2022.

⁵ <http://adams.dm.unipi.it/orbfit/>

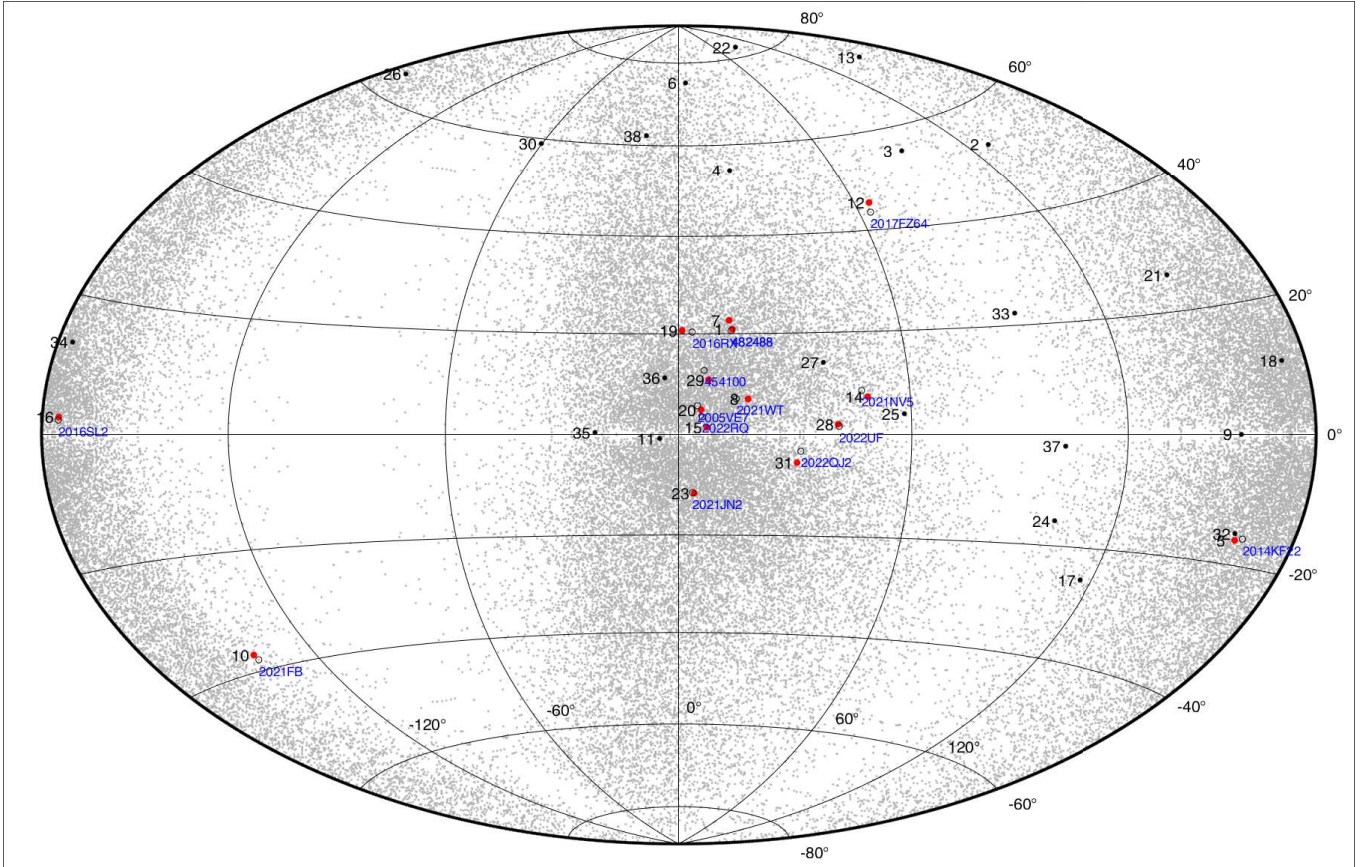


Figure 2. The true geocentric all-sky radiants distribution, for each meteorite identified by the numbers listed in Table A1 in an equal area projection of the sky centered on the Sun opposition; the angular coordinates are ecliptic longitude minus the longitude of the Sun, and ecliptic latitude. The gray dots are the distribution of the NEAs radiants intersecting the Earth’s orbit, the red dot are the meteorites with the candidate associated NEAs listed in Table 3, the circles are the corresponding best candidate progenitor. The meteorites Innisfree (3), Sariçiçek (22), Murrili (24), Ejby (25) and Cavezzo (33), are found in areas where the density of NEAs radiants is low and the possible association with NEAs statistically simpler.

currence of random associations. For this purpose, two populations of NEAs were considered: observed and randomized, both evolved in ω . As the value of D_N increases starting from low number, it is expected that the number of randomized NEAs associated with the observed meteorites will increase slower than the population of observed NEAs, because with the randomization we have erased the underlying evolution, if any. As D_N increases further, there will be a tendency to have the same number of associations between the real and random populations because the high value of the distance will make the spurious associations ever more numerous. In this way it is possible to estimate the maximum value of D_N above which the physical association NEA–meteorite begins to lose its meaning due to the large number of random associations (Rožek, Breiter & Jopek 2011).

The population of randomized NEAs evolved into ω was constructed starting from the observed one and considering U , θ and ϕ as independent variables and randomly adding the probability density of the analogous quantities present in the NEAs observed population intersecting the Earth in their ω cycle. The longitude of the Earth λ instead has been replaced by random values taken between 0 and 360 degrees, which is equivalent to randomizing the date of the encounter with the Earth.

Using the meteorites encounter conditions listed in Table A1 and computing D_N with both observed and random NEAs using Eq. (1), we see that the number of possible meteorite–NEA pairs for small

D_N values rises much faster for the real population than for the virtual one, while for high values of D_N the number of pairs tends to be similar, see Table 2. By generating different virtual populations, there may be random fluctuations in the number of meteorite–NEA pairs for small values of D_N , an expected behavior because the population consists of tens of thousands of virtual asteroids which may be closer to a meteorite’s radiant than the real population. The value beyond which the number of meteorite–NEA pairs for the real population suddenly rises and stable spurious associations start to appear is 0.05, a value that we can take as a limit. However, we took a slightly larger D_N value of 0.06, to be sure not to miss any potential meteorite–NEA pairs. In our case it will be the subsequent dynamic analysis of the orbits to establish the possible physical connection, so $D_{N_{\max}} = 0.06$. The values reported in Table 2 refer to a single virtual population, and we can see that they are affected by small number statistics: trying to extrapolate an upper D_N limit by fixing an exact small probability for a spurious association may not give an appropriate result. The choice of $D_{N_{\max}} = 0.06$ is a safer and conservative choice, and it is also consistent with the values found by Jopek, Valsecchi & Froeschlé (1999) for the similarity of pairs and triplets about 865 meteor radiants with $D_{N_{\max}} \approx 0.02 - 0.08$.

Table 2. Number of meteorite–NEA pairs for observed (Obs) and randomized (Rand) NEAs populations evolved in ω . In the last column the probability of having a true meteorite–NEA pair is estimated. As we see, spurious pairs start to appear for $D_N \geq 0.05$ but we took a slightly larger $D_{N_{\max}} = 0.06$ value to be sure not to miss any potential meteorite–NEA pairs.

$D_{N_{\max}}$	Obs	Rand	(Obs – Rand)/Obs
0.010	0	0	1.00
0.020	0	0	1.00
0.030	1	0	1.00
0.040	1	0	1.00
0.050	12	2	0.83
0.055	16	2	0.87
0.056	18	4	0.78
0.057	19	4	0.79
0.058	21	4	0.81
0.059	22	4	0.82
0.060	22	4	0.82
0.061	22	6	0.73
0.062	25	6	0.76
0.063	25	6	0.76
0.064	29	6	0.79
0.065	30	6	0.80
0.070	41	10	0.76
0.080	66	16	0.76
0.090	98	35	0.64
0.100	141	51	0.64

3 ASSOCIATION BETWEEN NEAS AND METEORITES

Now that we have established a maximum value of D_N beyond which it is not advisable to go, from Eq. (1) we can compute $D_N \leq 0.060$ from the meteorites of Table A1 with the NEAs population ω -evolved and we found the possible meteorite–NEAs associations given in Table 3: in total there are 20 possible meteorite–NEA pairs.

These candidate NEAs are mostly small, with diameters of a few tens of meters although there are also objects up to 1 km in diameter, and none of them have been physically characterized. The asteroids that have been observed from the photometric point of view are 482488, 2005 VE7 and 454100. The first two appear in the catalog of Solar System Objects extracted from the Sloan Digital Sky Survey (Sergeyev & Carry 2021). This catalog contains data on 1 032 357 Solar System objects (asteroids, Kuiper Belt Objects, and comets) that were classified in a scheme consistent with Bus-DeMeo taxonomy.

Asteroid 482488 is classified as U (unknown type), while for 2005 VE7 there are two distinct observations. In the first one, it has a 67% probability of being an S-type, in the second one it is classified as U. Asteroid (454100) 2013 BO73 is listed in the Asteroid Lightcurve Database (Warner et al. 2009) with a rotation period of about 1.1 h. Unfortunately, the photometric observations are incomplete and it is possible that the period is completely wrong. If confirmed, it would be a value well below the cohesionless spin-barrier value valid for rocky asteroids - about 2.2 h, see Carbognani (2017) - and 454100 would be a natural candidate for rotational disruption. So of all the asteroids in Table 3 only 2005 VE7 has a probability of being an S-type. For the others asteroids there are not useful information.

According to the Tisserand parameter with respect to Jupiter, all the progenitor candidates have asteroidal-type orbits except 2016 RX, which is just under three. In general, the orbits of meteorites in Table 3 tend to have a low inclination on the ecliptic except Pribram, Neuschwanstein, Bunburra, Jesenice and Annama which have inclinations higher than about 9° . At first glance, the

most interesting result is that Pribram and Neuschwanstein have the same NEA as a possible progenitor. This is not surprising considering that these two meteorites have a very similar orbit, a fact that was immediately noticed after the Neuschwanstein event (Spurný, Oberst & Heinlein 2003). Note that there are three meteorites, Hamburg, Košice and Križevci which are potentially associated with two NEAs at the same time, while Motopi Pan is associated with three NEAs. The best progenitor candidate of the meteoroid that produced Motopi Pan, the asteroid 454100, was also found by de la Fuente Marcos & de la Fuente Marcos (2019) using D-criteria.

The asteroids in Table 3 have low escape velocities, in the range $0.01-1 \text{ m s}^{-1}$ if we assume the typical average density for S-type asteroids of $2.72 \pm 0.54 \text{ g cm}^{-3}$ (Carry 2012). Therefore any physical mechanism invoked to extract a meteoroid from their surface must be able to impart at least a velocity higher than this range. In the case of an impact, statistically the larger ejecta have a slower velocity than the smaller ones which tend to travel further away from the impact site. The velocity of the ejecta falls approximately in the range $V \sim 10^{-4} - 10^{-1} U_i$, where U_i is the impact speed (Ferrari et al. 2022). Considering that the typical collision velocity between NEAs is of the order of $10-15 \text{ km s}^{-1}$ (Bottke, Nolan, & Greenberg 1993), we can expect ejecta velocities in the range $1.0 \text{ m s}^{-1} - 1.5 \text{ km s}^{-1}$ or at most of few km per second. About the rubble-pile rotational instability, by definition the expulsion occurs when the meteoroid on the NEA's surface exceeds the escape velocity (Jewitt 2012), while for tidal destruction by the Earth the relative velocity between the fragments can be estimated in the order of 1 m s^{-1} (Schunova et al. 2014). Finally, thermal fracturing of the surface rocks can lead to ejection speeds of the order of 20 m s^{-1} for a ΔT of about 1000 K (Jewitt 2012). All these speed values are equal or higher than the escape speeds of the NEAs in Table 3, therefore all these mechanisms are potentially able to cause a spatial separation between a NEA and its components. The ejection velocities are much smaller than NEAs orbital speed, so the orbits of the ejected meteoroid will be similar to that of the parent body. Only in the case of collisions, one can expect an ejection velocity much higher than the escape velocities, so in this case it is reasonable to expect a faster divergence between the orbits than in the other - less energetic - cases.

To verify if the candidate pairs in Table 3 have a real physical meaning, we checked the past orbital evolution of both meteorite and NEA. In fact, even if we chose $D_{N_{\max}}$ in such a way to avoid random associations as much as possible, the large number of NEAs and meteorites with low orbital inclination could make the association random anyway.

4 ORBITS EVOLUTION

Numerical integrations were performed with the mercury⁶ N-body code (Chambers & Migliorini 1997), by using the Bulirsch-Stoer integration method (Stoer & Bulirsch 2002). The dynamical model used for the propagation of the orbits was purely gravitational, and include the attraction of the Sun and the perturbations of the eight planets from Mercury to Neptune. Initial conditions of the planets at the epoch of a meteorite fall were computed with the OrbFit software, that includes a planetary ephemerides generator based on the JPL DE431 ephemerides system (Folkner et al. 2014).

Uncertainties of meteorite orbits are generally larger than those of

⁶ <https://github.com/Fenu24/mercury>

Table 3. List of meteorites with an associated NEA with $D_N \leq 0.06$. The column with Diam. is the estimated diameter, T_J is the Tisserand invariant with respect to Jupiter ($T_J < 3$ indicate a comet-like orbit), while the column with C is a value from the NEOCC database between 0 and 9 indicating how well an object’s orbit is known on a logarithmic scale, where 0 indicates a well-determined orbit.

Meteorite Name	NEA	Diam. (m)	T_J	C	D_N
Pribram	482488	300–600	3.109	0.3	0.047
Peekskill	2014 KF22	15–30	4.444	5.9	0.041
Neuschwanstein	482488	300–600	3.109	0.3	0.056
Park Forest	2021 WT	30–60	3.178	7.6	0.053
Bunburra Rockhole	2021 FB	20–40	6.942	6.4	0.042
Jesenice	2017 FZ64	40–100	3.736	7.8	0.055
Košice	2021 NV5	10–20	3.234	6.8	0.049
	2019 ST2	50–120	3.288	9.0	0.059
Križevci	2022 RQ	20–50	4.472	7.9	0.044
	2013 BR15	30–60	4.280	9.0	0.056
Sutter’s Mill	2016 SL2	30–60	3.327	8.7	0.050
Annama	2016 RX	20–40	2.943	7.1	0.048
Žd’ár nad Sázavou	2005 VE7	500–1200	3.156	0.5	0.048
Creston	2021 JN2	40–100	5.328	7.0	0.055
Hamburg	2022 UF	10–20	3.110	6.8	0.057
	2021 PZ1	20–40	3.279	7.6	0.043
Motopi Pan	454100	500–600	4.824	0	0.044
	2017 MC3	40–100	4.333	3.5	0.046
	2009 FZ4	20–50	5.535	2.0	0.055
Arpu Kuilpu	2022 QJ2	20–50	3.067	8.2	0.057

NEAs orbits, because meteorites are observed only in a really short interval of time during the fall. To take into account such uncertainties and provide a deeper analysis of the correlation between a meteorite and a potential progenitor NEA, we produced orbital clones of the meteorite. To this purpose, we assumed that each orbital element is Gaussian distributed, with a mean value corresponding to the nominal value and a standard deviation equal to the 1σ uncertainty (see Table 1).

The mean anomaly M was computed by using the Kepler equation with the true anomaly f at the epoch of the fall, that is determined only by the geometry of the orbit and the position along it as follows:

$$f = \begin{cases} -\omega & \text{asc. node fall, } \omega < 180^\circ, \\ 180^\circ - \omega & \text{des. node fall, } \omega < 180^\circ, \\ 360^\circ - \omega & \text{asc. node fall, } \omega > 180^\circ, \\ 180^\circ - \omega & \text{des. node fall, } \omega > 180^\circ. \end{cases} \quad (8)$$

Equation (8) is a geometric relation between the true anomaly f at the time of passage through the ascending or descending node, and the argument of perihelion ω that does not involve the semi-major axis of the orbit. Note that the fall necessarily happens at the passage through the node. As a test, we verified that the value of the mean anomaly M for Almahata Sitta (due to the fall of asteroid 2008 TC3) and Motopi Pan (due to the fall of 2018 LA), see Table 1, was in good agreement with the value given by JPL Small- Body Database⁷. The 1σ uncertainty in the mean anomaly M was assumed to be the same as the 1σ uncertainty in ω .

For the meteorites of Table 3 with an identified candidate progenitor, we simulated the backward evolution of 5000 orbital clones. The orbits were propagated from the epoch of the fall to 100 kyr

prior the fall, by using a maximum timestep of 0.5 days. Output orbital elements were recorded every 50 yr. The nominal orbit of the NEA progenitor was also integrated backwards for the same timespan and with the same dynamical model. Keplerian initial conditions of NEAs of Table 3 at epoch 2460000.5 JD were taken for the NEOCC portal⁸, and are also reported in Table A2.

4.1 Pribram–482488 and Neuschwanstein–482488

We first analyze the possible correlation between the Pribram and Neuschwanstein meteorites and the NEA 482488. Babadzhinov, Williams & Kokhirova (2012) identified the meteor showers associated with 2004CK39 by taking as an indicator the time evolution in the planes (ω, R_a) and (ω, R_d) , where

$$R_a = \frac{a(1 - e^2)}{1 + e \cos \omega}, \quad R_d = \frac{a(1 - e^2)}{1 - e \cos \omega}, \quad (9)$$

are the ascending and descending node distances. This is done because the time evolution of R_a, R_d could be very different between the meteorite and the candidate NEA progenitor. In Babadzhinov, Williams & Kokhirova (2012), the authors found similar evolutionary paths for the NEA and the meteor showers, and they therefore suggested a possible correlation. We followed a similar approach to provide an evidence of the common origin of the Pribram and the Neuschwanstein meteorites through the NEA 482488. Because the backward evolution of a meteorite orbit is propagated using orbital clones, we took into account the density distribution in the planes (ω, R_a) and (ω, R_d) , computed over the whole 5000 orbits. Figure 3 shows the density plots for the two pairs Pribram–482488 and Neuschwanstein–482488. The path of the nominal orbit of the NEA, depicted with green dots, is superimposed on the density plots. In both cases, the evolution of 482488 follows almost exactly the areas with the largest density, denoted by the orange color. This already provides a first indication of the common origin of these objects.

To understand whether it is possible to determine a candidate age for the separation between the meteorite and the proposed parent body, we searched for convergence events involving a small relative velocity and a small distance between the two objects. To this purpose, we adopted an approach similar to that used by Moskovitz et al. (2019) to study the two NEAs asteroid pairs 2015 EE7–2015 FP124 and 2017 SN16–2018 RY7. The distance was evaluated in terms of the Minimum Orbit Intersection Distance (MOID) between the orbit of the meteorites and that of 482488, while for the velocity we considered the norm of the difference between the heliocentric velocities. Since the errors in the initial orbital elements are typically accumulated in the mean anomaly in long-term numerical propagation, the instantaneous relative velocity is not very informative for the purpose of finding a possible separation age. Instead, we considered the relative velocity ΔV at the mean anomaly that realizes the MOID. At the separation event, we expect both the MOID and the relative velocity to be small. To find such events, we computed the dimensionless distance

$$d = \sqrt{\left(\frac{\text{MOID}}{\mu(\text{MOID})}\right)^2 + \left(\frac{\Delta V}{\mu(\Delta V)}\right)^2}, \quad (10)$$

where $\mu(\text{MOID})$ and $\mu(\Delta V)$ are the median values of the MOID and the relative velocity at the MOID, respectively, computed over the whole integration timespan. For each clone, we recorded the

⁷ <https://ssd.jpl.nasa.gov/>

⁸ <https://neo.ssa.esa.int/>

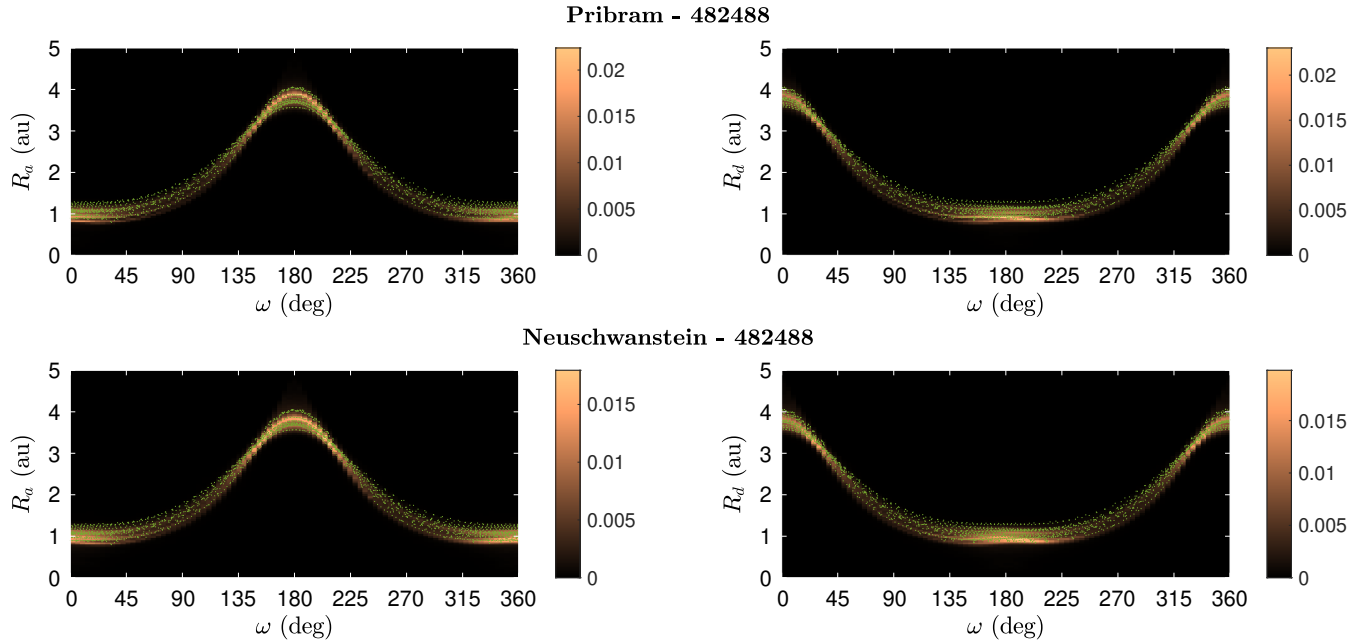


Figure 3. Evolution in the planes (ω, R_a) (left column) and (ω, R_d) (right column), for the pairs Pribram–482488 (first row) and Neuschwanstein–482488 (second row). The green dots denote the evolution of the NEA parent body 482488. The evolution of the meteorite orbital clones is shown as a density plot, computed over the whole 5000 orbits.

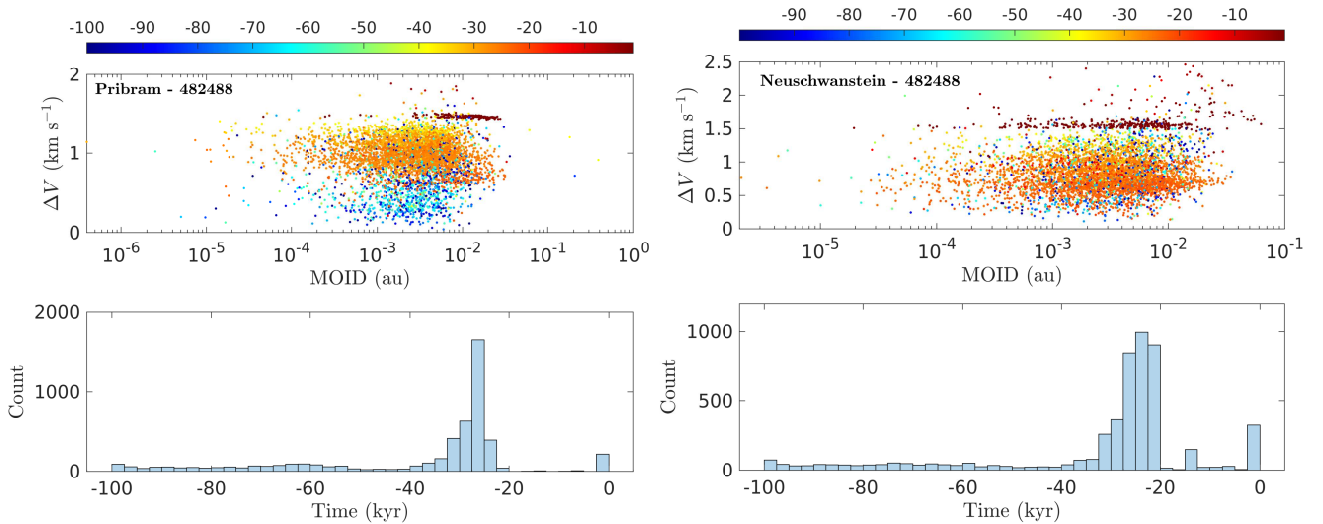


Figure 4. Distributions of the relative velocity vs. the MOID at the time t_{\min} (first row), and histogram of t_{\min} (second row).

Plots in the left column refer to the pair Pribram–482488, while those of the right column to Neuschwanstein–482488. The unit for the colorbar in the first row is kyr. The bins in the histograms of the second row have a constant width of 2.5 kyr.

minimum d_{\min} of the distance d and the corresponding time t_{\min} , together with the values of the MOID and ΔV attained at t_{\min} .

Figure 4 shows the distribution of the MOID and ΔV (first row) and that of the time t_{\min} (second row). Plots on the left column refer to the pair Pribram–482488, while those on the right column to Neuschwanstein–482488. In both cases, we can note accumulations of the MOID at values smaller than 0.1 au during the first 5 kyr of backwards evolution, happening at a relative velocity of $\sim 1.5 \text{ km s}^{-1}$. In addition, a large concentration of minima are found for MOID between 10^{-4} au and 10^{-5} au at relative velocities of $\sim 1 \text{ km s}^{-1}$ for the pair Pribram–482488, and smaller than $\sim 1 \text{ km}$

s^{-1} for Neuschwanstein–482488. Some isolated points of the distribution extend even towards $\text{MOID} \sim 10^{-5}$ au and $\Delta V \sim 0.5 \text{ km s}^{-1}$. These large concentrations happen mostly between -25 and -30 kyr for Pribram–482488 and between -20 and -25 kyr for Neuschwanstein–482488. Beyond -40 kyr of evolution we cannot distinguish anymore any clear concentrations of small MOID and small ΔV , and we believe this to be caused by both the chaotic nature and the uncertainties of the orbits of the meteorites, and an identification of a separation event dating further back is not possible in these cases. Even if the relative velocities did not reach very low values of the order of few tens of m s^{-1} as found in the NEAs pairs

by Moskovitz et al. (2019), they still may suggest that the Pribram and Neuschwanstein both originated from 482488, and the peaks in the distributions of t_{\min} would suggest a separation age between -20 and -30 kyr.

These are the results that can be obtained from a dynamical point of view. If we consider the cosmic-ray exposure age of the two meteorites we see that they differ: for Pribram it is estimated in 12 Myr, while for Neuschwanstein it is around 48 Myr (Spurný, Oberst & Heinlein 2003). However, the cosmic-ray exposure time of a meteorite does not necessarily coincide with the time spent in space by the original meteoroid, rather it is the time period in which the meteorite was bombarded by cosmic rays, which can also occur up to about one meter below the surface of the progenitor body (Eugster 2003). This condition can occur if the progenitor NEA is, for example, a rubble pile, as can be 482488. In this case it is reasonable to expect that the asteroid is composed of fragments with a not coincident cosmic-ray exposure history.

4.1.1 Influence of the Yarkovsky effect

For these two pairs of meteorite–NEA we performed additional simulations that included the Yarkovsky effect in the orbital evolution. The pre-atmospheric mass of Neuschwanstein was estimated to be about 300 ± 100 kg (Spurný, Oberst & Heinlein 2003), corresponding to a diameter of about 0.55 meters assuming a measured mean density $\rho \approx 3.5$ g cm $^{-3}$ (Flynn et al. 2018). It is reasonable to assume that Pribram was also similar in size and mass. To estimate the semi-major axis drift caused by the Yarkovsky effect we used the calibration based on Bennu (Spoto, Milani & Knežević 2015) given by

$$\left(\frac{da}{dt}\right) = \left(\frac{da}{dt}\right)_B \times \frac{\sqrt{a_B}(1 - e_B^2)}{\sqrt{a}(1 - e^2)} \frac{D_B \rho_B \cos \gamma}{D \rho \cos \gamma_B} \frac{1 - A}{1 - A_B}, \quad (11)$$

where ρ is the density, D is the diameter, γ is the obliquity, and A is the Bond albedo. The subscript B denotes the values corresponding to asteroid Bennu, and a summary of the numerical values can be found for instance in Del Vigna et al. (2018). For the meteorite, we used $\rho = 3.5$ g cm $^{-3}$, $D = 0.55$ m and $\gamma = 180^\circ$, obtaining a semi-major axis drift of $da/dt = -0.64$ au My $^{-1}$, that we maintained constant through the whole integration time-span. Numerical integrations were performed with a modified version of the mercury integrator (Fenucci & Novaković 2022), by using the same orbital clones used for the previous simulations. The evolution in the planes (ω, R_a) and (ω, R_d) was not affected by the introduction of the Yarkovsky effect in the model, and therefore it is not reported.

On the other hand, both the distributions of the values of the MOID and the relative velocities ΔV at the minima of d , and that of t_{\min} , show differences with respect to those obtained in a purely gravitational model (see Fig. 5). A larger concentration of points at velocities $\Delta V \sim 1.5$ km s $^{-1}$ can be seen in the simulations that included the Yarkovsky effect in the model, happening during the first 2.5 kyr of backward evolution, thus producing a new more prominent peak in the distribution of t_{\min} . On the other hand, the peaks between -20 and -30 kyr are still present, suggesting that the proximity result between the orbits of the meteorites and that of 482488 is robust. It is important to note that the semi-major axis drift estimate obtained by Eq. (11) is the maximum drift that can be obtained, because we fixed the obliquity to 180° . However, the Yarkovsky effect may result to be much smaller for different reasons. A first reason is that the diurnal Yarkovsky effect is proportional to $\cos \gamma$, hence this component is not effective at obliquity equal to 90° . A second reason is that the rotation period of small asteroids can reach very small values of the order of

few seconds (Pravec & Harris 2000), causing the thermal re-emission to be isotropic and hence slowing down the net Yarkovsky effect. Finally, the Yarkovsky–O’Keefe–Radzievskii–Paddack (YORP) effect (Rubincam 2000; Bottke et al. 2006) is another thermal effect strictly related to the Yarkovsky effect, that causes a time evolution of both the obliquity and the rotation period. The magnitude of this effect scales as $1/D^2$, and the YORP cycle (i.e. the time needed to reach one of the asymptotic obliquity values of $0^\circ, 90^\circ$ or 180°) can be very short for meter-sized objects. This causes a random walk in the semi-major axis drift da/dt (Bottke et al. 2015), thus decreasing the total average drift. The simulation presented here represents the most extreme case, in which the Yarkovsky effect is maximum and it is kept at the same value for the whole duration of the integration timespan, hence it is reasonable to assume that the results we obtained in the purely gravitational case are stable also in the case of smaller semi-major axis drifts.

In the following sections we use similar methods to those used here to discuss the possible confirmation of the meteorites–NEAs pairs of Table 3, except for the inclusion of the Yarkovsky effect in the model.

4.2 Annama–2016 RX

Compared with the cases examined in Sec. 4.1, the evolution of the the nodal distances R_a and R_d as a function of ω covers a larger dense area (see Fig. 6, first row). This is caused mainly by a quite large 1σ uncertainty of 0.12 au in the semi-major axis of the orbit of the Annama meteorite (see Table 1). The path followed by 2016 RX (green curve in Fig. 6) shows some deviations from the path followed by the meteorite clones, especially near $\omega = 180^\circ$ for the ascending node and near $\omega = 0^\circ$ for the descending node. Moreover, a chaotic behaviour of the nominal orbit of 2016RX happening after several thousands of years of evolution can be seen. The first panel of Fig. 7 shows the distribution of the MOID and the relative velocity ΔV at the minima of the distance d of Eq. (10). Two separated concentrations of points stand out in the distribution: one at $\Delta V \sim 4$ km s $^{-1}$ and another one at $\Delta V < 4$ km s $^{-1}$, both spanning values of the MOID from ~ 0.1 au down to 10^{-4} au. The minima at higher relative velocity are realized by about half of the clones within the first 2.5 ky of dynamical evolution, before strong chaotic dynamical effects are able to significantly change the secular evolution. On the other hand, the minima with smaller relative velocity appear to be concentrated at about -35 kyr, and they show a larger dispersion in ΔV . The two peaks in the time t_{\min} suggest two possible separation epochs, and the values of the ΔV appear to be compatible with a collisional origin.

4.3 Bunburra Rockhole–2021 FB

The evolution in the planes (R_a, ω) and (R_d, ω) are shown in the second row of Fig. 6. The evolution of the possible parent body 2021 FB follows the densest area produced by the orbital clones of the Bunburra Rockhole meteorites, and the nodal distances do not show large variations during the secular evolution. Note also that the nominal orbital elements of 2021 FB (see Table A2) are very close to that of the Bunburra Rockhole meteorite. The distribution of MOID and ΔV at the minimum of d , and the distribution of t_{\min} , are shown in Fig. 7, third and fourth panels, respectively. A concentration of minima at MOID ~ 0.05 – 0.07 au and $\Delta V \sim 3$ km s $^{-1}$ can be seen in the distribution, and they are realized within the first 2.5 kyr of backward evolution by about ~ 800 clones. After this initial period of

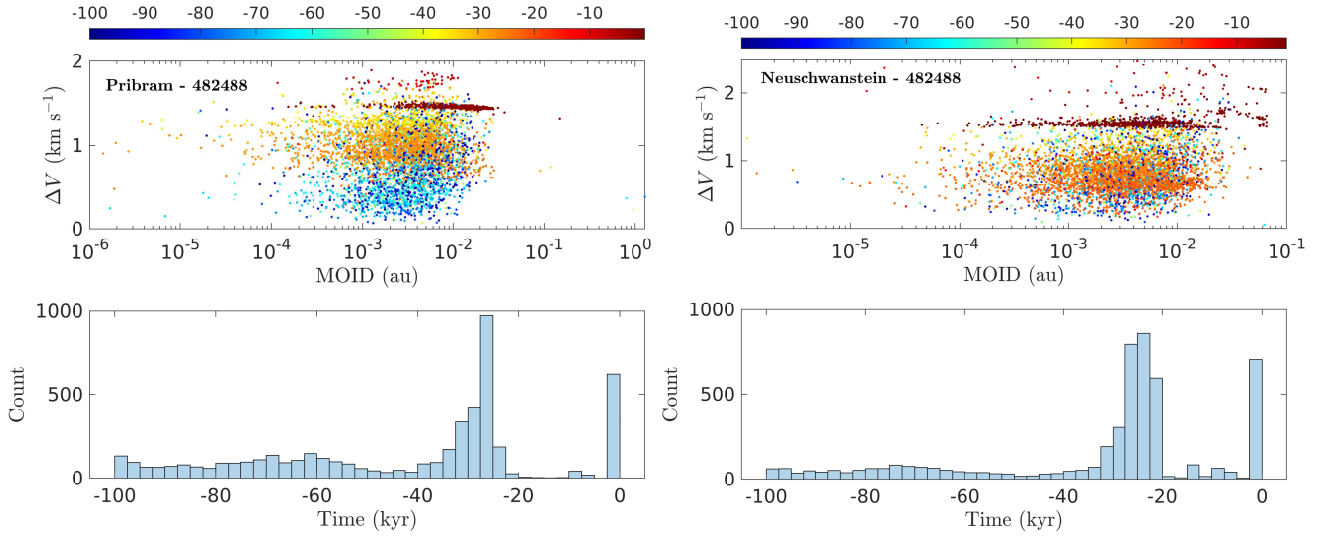


Figure 5. Same as Fig. 3 for the simulations performed by including the Yarkovsky effect in the model.

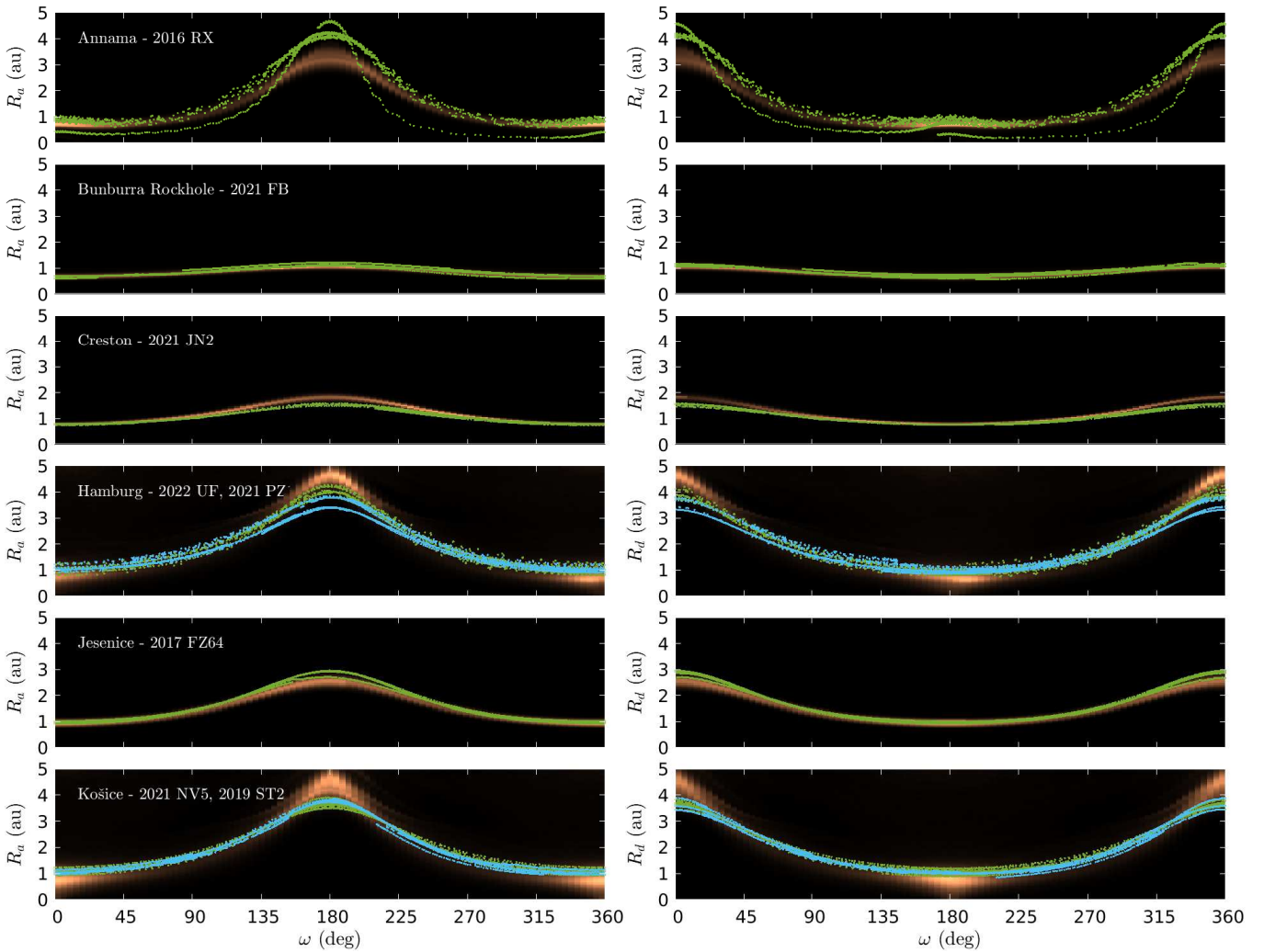


Figure 6. Same as Fig. 3 for the pairs Annama–2016 RX (first row), Bunburra Rockhole–2021 FB (second row), Creston–2021 JN2 (third row), Hamburg–2022 UF, 2021 PZ1 (fourth row), Jesenice–2017 FZ64 (fifth row), and Košice–2021 NV5, 2019 ST2 (sixth row). The green color represents the evolution of the primary associated NEA, and the cyan color the evolution of the secondary associated NEA, when present.

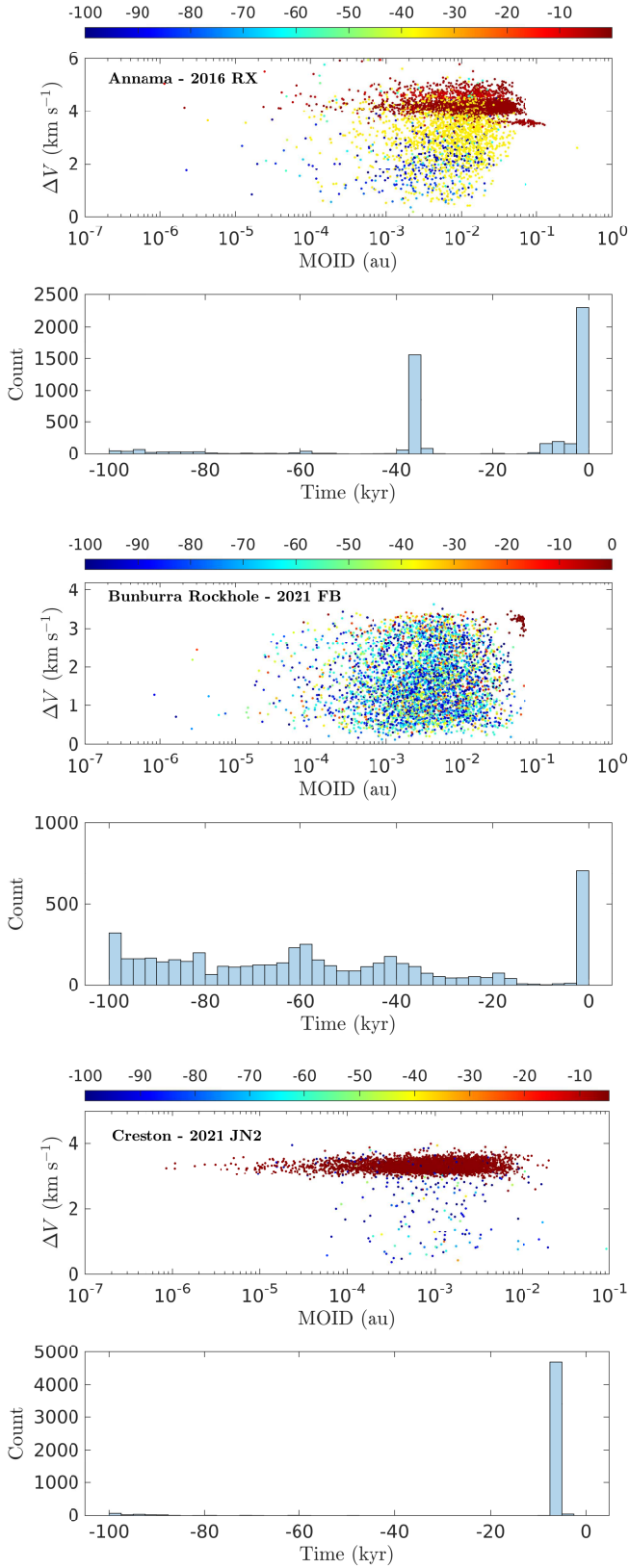


Figure 7. Distributions of the relative velocity vs. the MOID at the time t_{\min} and distribution of t_{\min} , for the pairs Annama–2016 RX, Bunburra Rockhole–2021 FB, and Creston–2021 JN2.

evolution, the minima appear to be almost uniformly spread in time, without showing any clear concentration. This is probably caused by strong chaotic effects dominating the secular dynamics, since these objects are placed inside the orbit of the Earth at relatively low inclination. Despite the concentration of minima of d in the first 2.5 kyr, the relatively large values of the MOID suggest that this association is more likely to be spurious. In fact, Bunburra Rockhole is an Eucrite meteorite most likely coming from the innermost region of the main belt, and supposedly delivered through the ν_6 secular resonance (Bland et al. 2009).

4.4 Creston–2021 JN2

The evolution of the candidate NEA parent body 2021 JN2 in the planes (R_a, ω) and (R_d, ω) shows a good agreement with the densest area traced by the orbital clones of the Creston meteorite (see Fig. 6, third row). As seen in the previous section, this is already an indication of a possible correlation between the two bodies. Figure 7 shows the distribution of the MOID and the relative velocity ΔV at the minima of the distance d , together with the times t_{\min} at which the minima are realized. The outstanding feature of these two distributions is that almost all the minima are concentrated at $\Delta V \sim 3.5 \text{ km s}^{-1}$, with MOID spanning values between 0.01 au and 10^{-6} au. Moreover, all the minima are realized between -5 and -7.5 kys of dynamical evolution, that is likely small enough to ensure that the chaotic nature of the long term dynamics has not become prevalent. More extensive and accurate numerical simulations, that are beyond the scope of this work, would be needed to better assess the results presented here about this pair, possibly taking into account also the uncertainties in the orbit of the NEA parent body. The values of the relative velocity may be an indication that the Creston meteorite was formed by an impact on 2021JN2, however further observations and physical characterization would be needed to better explore this hypothesis.

4.5 Hamburg–2022UF, 2021 PZ1

The fourth row of Fig. 6 shows the density plot of the Hamburg meteorite clones in the planes (ω, R_a) and (ω, R_d) , together with the path followed by the corresponding NEA parent body candidates. The primary 2022 UF is shown by green dots while the secondary 2021 PZ1 is represented by cyan dots. The candidate parent bodies and the meteorite clones have a similar qualitative evolution. However, we can see significant differences of more than 1 au between the ascending node R_a of the two NEAs and the densest area of the meteorite clones distribution at $\omega = 180^\circ$, where R_a is at the maximum. At $\omega = 0^\circ$, where R_a is at the minimum, the orbit of the NEAs is also a bit off of the densest part of the distribution, of about ~ 0.5 au. Similar features can be seen also in the descending node R_d at $\omega = 0^\circ$, where the nodal distance is at the maximum and the differences are of about ~ 1 au, and at $\omega = 180^\circ$, where R_d is at the minimum and the offset is of about ~ 0.5 au.

In addition, we noted that 1591 clones of the Hamburg meteorite were expelled from the Solar System during the 100 kyr of backward evolution. The orbits of the clones are close to the 5:2 mean-motion resonance with Jupiter, that may be responsible of increasing the eccentricity sufficiently enough to put them on Jupiter crossing orbits and, in fact, the clones were ejected by effect of close encounters with Jupiter. We found that the distribution of the ejection times is fairly constant between -10 kyr and -100 kyr. This suggests that these orbits begin to be chaotic after a few kyr of dynamical evolution,

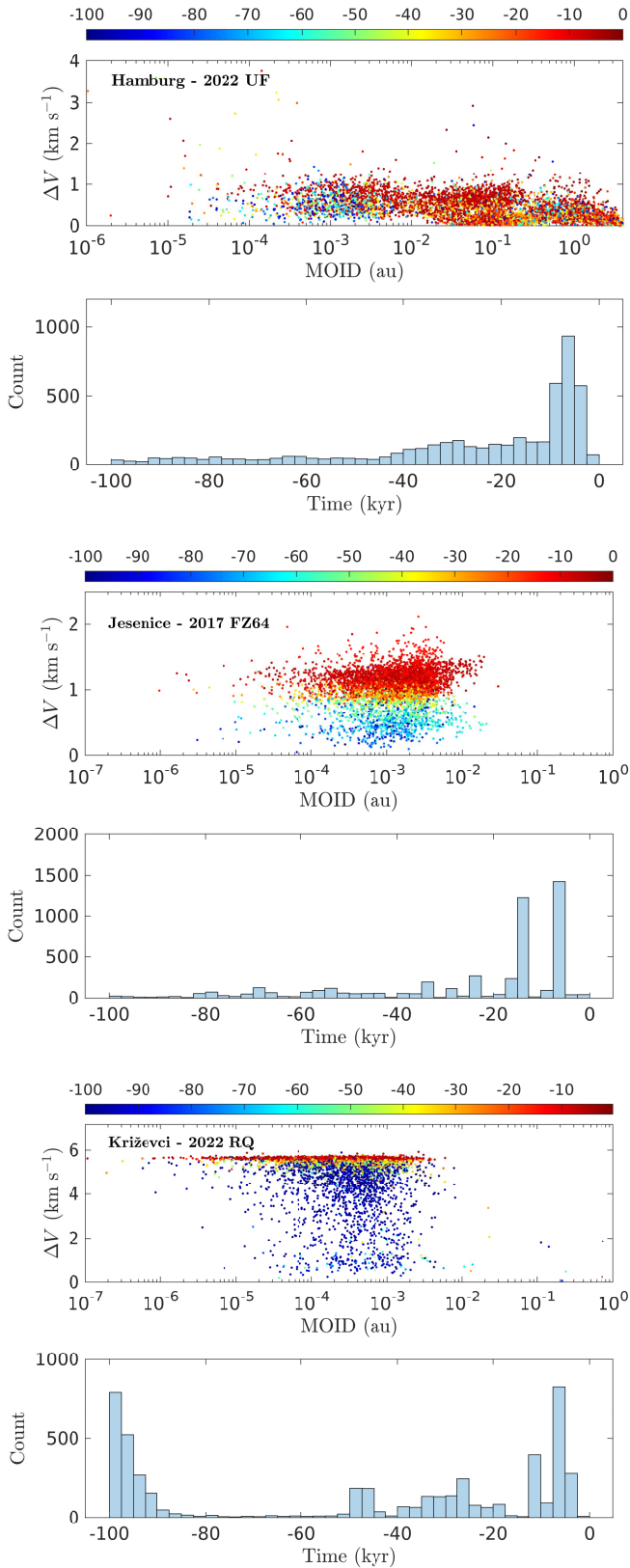


Figure 8. Distributions of the relative velocity vs. the MOID at the time t_{\min} and distribution of t_{\min} , for the pairs Hamburg–2022 UF, Jesenice–2017 FZ64, and Križevci–2022 RQ.

making the attempt to identify their parent body of the Hamburg meteorite harder, unless the separation age happened only very recently. The distribution of the MOID and the relative velocity at the minima of d for the pair Hamburg–2022 UF does show a concentration at $\Delta V < 1 \text{ km s}^{-1}$ happened during the first 10 kyr of dynamical evolution, before the start of the chaotic dynamical regime. The values of the MOID span a large interval of values, from $\sim 0.3 \text{ au}$ down to $\sim 10^{-4} \text{ au}$, indicating that some of the meteorite clones arrive close enough to 2022 UF to suggest a possible common origin. On the contrary, the distribution for the pair Hamburg–2021 PZ1 does not show any concentration of points, and the times t_{\min} are constantly distributed through the whole 100 kyr of dynamical evolution (see Fig. A1). Therefore, we believe this association to be spurious. As demonstrated by this case, and from others in the following sections, having a small value of D_N is not enough to conclude the correlation, but further numerical simulations of the past evolution need to be performed. Note that an older separation event cannot be ruled out at this stage, however such simulations would require a more careful modeling of the dynamics that is out of the scope of this work.

Apart from the chaotic nature of this specific case, the approach we used to find possible parent bodies may not give appropriate results in presence of objects that are placed deep inside a mean-motion resonance with Jupiter. Indeed, the method by Gronchi & Milani (2001) to compute the secular evolution of NEAs is valid under the assumption that no mean-motion resonances between the asteroid and a planet are present. High-order mean-motion resonances or mean-motion resonances with the inner planets may still not cause appreciable differences in the secular evolution. However, low-order mean-motion resonances with Jupiter are strong enough to significantly change the secular evolution, and another model for the secular propagation has to be used (Fenucci, Gronchi & Sillenfest 2022). Currently, the identification and the computation of proper elements for resonant NEAs is not automatized, and searching for possible parent bodies taking into account this additional dynamical aspect is beyond the purpose of this work.

4.6 Jesenice–2017 FZ64

Figure 6, fifth row shows the evolution in the planes (R_a, ω) and (R_d, ω) . As in the previous cases, the evolution of the candidate NEA parent body agrees with that of the meteorite clones. The distributions of the MOID and ΔV at the minima of d , as well as that of t_{\min} (see Fig. 8, third and fourth panels), show similar features to those of the pair Annama–2016 RX presented in Sec. 4.2. The distribution of t_{\min} has two sharp peaks at about -10 kyr and -17 kyr , with the first peak realized by about 1500 orbital clones and the second one by about 1200 orbital clones, indicating two possible separation epochs. The minima are concentrated at relative velocities of $\sim 1 \text{ km s}^{-1}$, while the MOID spans values up to 0.02 au down to 10^{-5} au . Note that the values of relative velocity are still compatible with an impact origin.

4.7 Košice–2021 NV5, 2019 ST2

The sixth row of Fig. 6 shows the density plots in the planes (ω, R_a) and (ω, R_d) , together with the path followed by the NEA parent body candidates 2021 NV5 and 2019 ST2 in green and cyan, respectively. This case is qualitatively similar to that of the pair Hamburg–2022 UF, 2021 PZ1 discussed in Sec. 4.5, therefore we refer to the relative paragraph for the description of this aspect. In addition, 1180 orbital clones of the Košice meteorite were expelled from the Solar System,

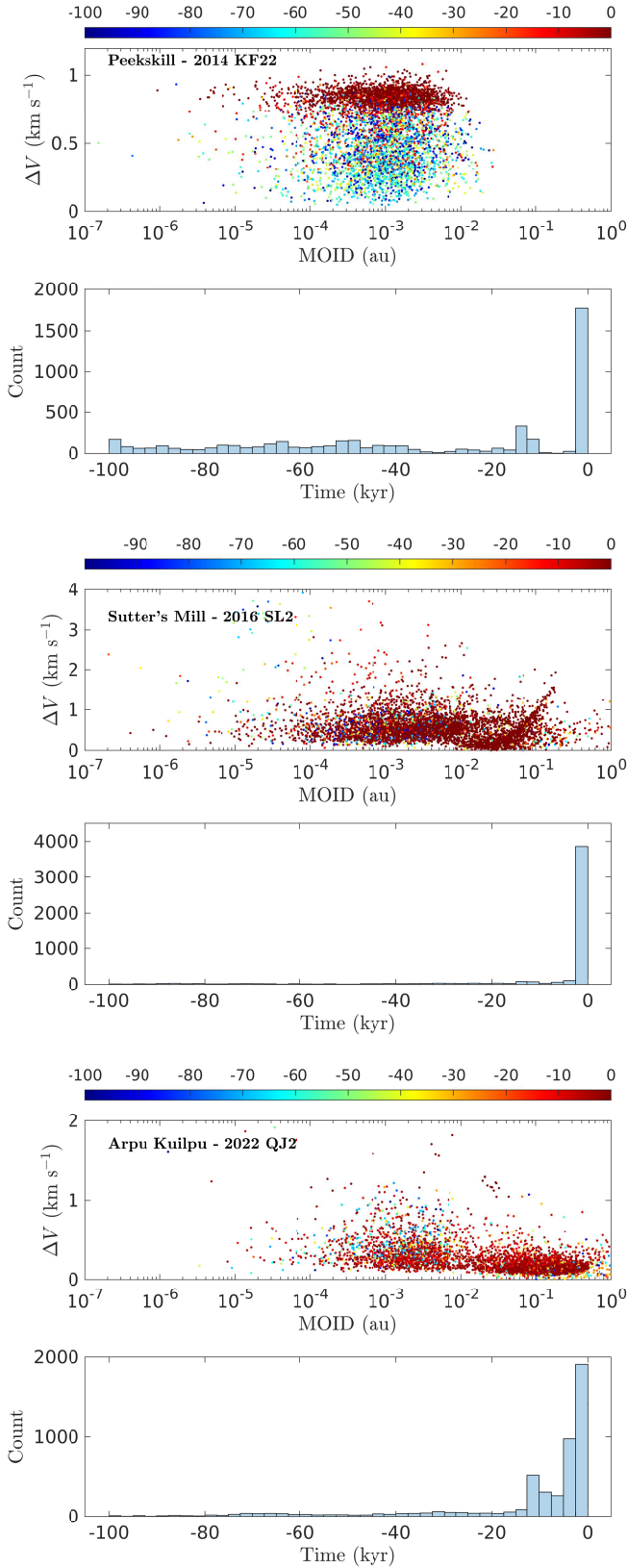


Figure 9. Distributions of the relative velocity vs. the MOID at the time t_{\min} and distribution of t_{\min} , for the pairs Peekskill–2014 KF22, Sutter’s Mill–2016 SL2, and Arpu Kuilpu–2022 QJ2.

again probably by the effect of the 5:2 mean-motion resonance with Jupiter, with ejection times almost equally distributed between -10 kyr and -100 kyr. However, differently from the case of the Hamburg meteorite, we did not find any concentration of minima of d before the beginning of the chaotic dynamics phase, for both the candidate parent bodies 2021 NV5 and 2019 ST2. For the distributions of the relative velocity vs. the MOID at the time t_{\min} and distribution of t_{\min} , see Fig. A1. Therefore, we cannot give any strong evidence for a true correlation of these objects. According to Borovička et al. (2013) the origin of the Košice meteoroid is in the central main asteroid belt near the 8:3 main motion resonance with Jupiter.

4.8 Križevci–2022 RQ, 2013 BR15

The secular evolution of 2022 RQ and 2013 BR15 in the planes (R_a, ω) and (R_d, ω) are depicted in the first row of Fig. 10, with green and cyan colors respectively. The evolution of both these NEAs follow the densest area covered by the orbital clones of the Križevci meteorite. Figure 8 shows the distribution of the MOID and ΔV at the minima of d for the pair Križevci–2022 RQ, and a concentration of about 1000 points at about -7.5 kyr, gathered at $\Delta V \sim 6 \text{ km s}^{-1}$, can be recognized. Other concentrations of minima of d can be seen at times near -100 kyr, that can be attributed to the scattering of orbital elements due to chaos, and therefore probably not related to a true separation event. The relative velocity of almost 6 km s^{-1} may be an indication that the separation occurred because of an impact with a comparatively high relative velocity, although the possibility of a random association between the meteorite and NEA cannot be totally ruled out.

The same analysis performed for the pair Križevci–2013 BR15 showed that the minima of d are all concentrated at -100 kyr, except for about 300 clones that had a minima at about -17 kyr with relative velocity of 6 km s^{-1} (see Fig. A1). While this last mentioned concentration may be an indication of a separation induced by an impact, the small number statistics makes the conclusion of a true correlation between these bodies questionable, and therefore we tend to favor the random association hypothesis.

4.9 Park Forest–2021 WT

The secular evolution of 2021 WT follows exactly the same evolution of the clones of the Park Forest meteorite in the planes (R_a, ω) and (R_d, ω) , as shown in Fig. 10, second row. However, the distribution of the minima of d in the plane (MOID, ΔV) did not show any concentration of points, and the distribution of the times t_{\min} did not have any concentration of times (see Fig. A1), suggesting that this was a random spurious association. Note that the Park Forest meteorite falls in a region of the plane (θ, ϕ) that is quite filled by known NEAs (see Fig. 2), providing an additional evidence of the spurious association hypothesis.

4.10 Peekskill–2014 FK22

The evolution of the nodal distances as a function of ω for the pair Peekskill–2014 KF22 are shown in the third row of Fig. 10. Due to the small uncertainties in the orbit of the Peekskill meteorite, the densest area covered by the meteorite clones results to be very narrow. The path of the candidate parent body 2014 FK22 follows almost exactly the same corridor indicated by the meteorite clones, suggesting already a possible common origin.

Figure 9, first panel, shows the distribution of the MOID and ΔV

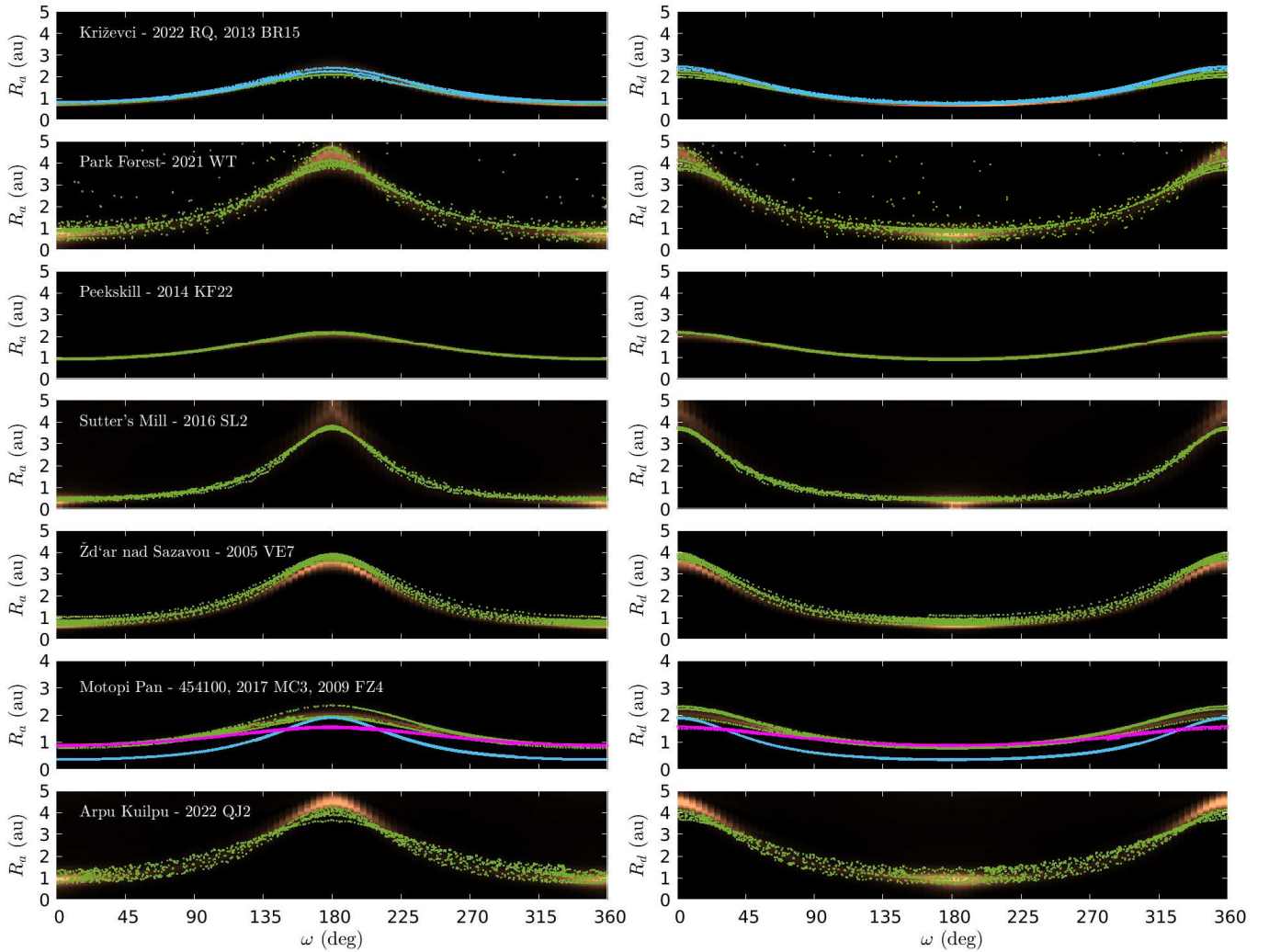


Figure 10. Same as Fig. 3 for the pairs Košice–2021 NV5, 2019 ST2 (first row), Križevci–2022 RQ, 2013 BR15 (second row), Park Forest–2021 WT (third row), Peekskill–2014 FK22 (fourth row), Sutter’s Mill–2016 SL2 (fifth row), and Žďár nad Sázavou–2005 VE7 (sixth row). The green color represents the evolution of the primary associated NEA, and the cyan color the evolution of the secondary associated NEA, when present.

at the MOID for the minima of the distance d . The relative velocities are all smaller than 1 km s^{-1} , and a concentration of points appears at values of the MOID between 10^{-2} and 10^{-5} au, with relative velocities at around 0.8 km s^{-1} . The distribution of t_{\min} is reported in the second panel of Fig. 9 and it shows a peak in the first 2.5 kyr of backward evolution, suggesting a really recent separation.

4.11 Sutter’s Mill–2016 SL2

The evolution of the Sutter’s Mill meteorite clones show some dispersion in the planes (R_a, ω) and (R_d, ω) (see Fig. 10, fourth row), probably due to the relatively large uncertainties on the orbital elements (see Table 1). Despite this, the evolution of 2016 SL2 is still compatible with that of the meteorite clones. Moreover, the distribution of t_{\min} (see Fig. 9) shows a concentration of 4000 orbital clones in the first 2.5 kys of backward evolution, thus likely before the beginning of the chaotic phase of the long term dynamics. The values of the MOID span an interval between 10^{-5} au up to 0.1 au, with relative velocities concentrated mostly at $\Delta V < 1 \text{ km s}^{-1}$. These values of ΔV are compatible with either a collisional origin or an ejection by YORP spin-up, however it is not possible to conclude

a clear preference among the two possibilities due to the lack of data about the lightcurve of the candidate NEA parent body. As for the case of Creston–2021 JN2 presented in Sec. 4.4, further more accurate numerical simulations should be performed to deeply assess the relation between these two objects.

4.12 Žďár nad Sázavou–2005 VE7

As in almost all the previous cases, the path of the NEA candidate parent body follows the densest area of the meteorite clones in the planes (R_a, ω) and (R_d, ω) , see Fig. 10 fifth row. However, the distribution of MOID and ΔV at the minima of the distance d do not show any clear accumulation of points at low velocity. The histograms of t_{\min} (not shown in the paper) look almost equi-distributed throughout the first 80 kyr of backward dynamical evolution, showing a peak only near epoch -100 kyr. In this case, the concentration at such large epoch in the past is mostly due to the scattered dynamics induced by chaos, rather than from a true separation event, and therefore we cannot conclude a possible correlation for this pair. For the distributions of the relative velocity vs. the MOID at the time t_{\min} and distribution of t_{\min} , see Fig. A1.

4.13 Motopi Pan–454100, 2017 MC3, 2009 FZ4

Motopi Pan is the only meteorite for which we found three candidate parent bodies. Figure 10, sixth row, shows the evolution of the nodal distances R_a and R_d as a function of ω of the meteorite clones. The evolution of the same quantities of the candidate parent bodies 454100, 2017 MC3, and 2009 FZ4 are superimposed with green, cyan, and magenta dots, respectively. The best match is achieved by 454100, that follows very precisely the densest area given by the meteorite clones. The asteroid 2009 FZ4 also shows a good agreement in the evolution of the nodal distances, except near $\omega = 180^\circ$ for the ascending nodal distance and near $\omega = 0^\circ$ for the descending nodal distance. On the other hand, the evolution of 2017 MC results to be qualitatively different, and the crossing configurations with the Earth orbit happening at $R_a, R_d = 1$ au happen at values of ω much different from the other two cases.

Figure 11 shows the evolution of MOID and ΔV at the minima of d , and the histograms of the time t_{\min} for the three pairs. The minima for the couple Motopi Pan–454100 are all notably constrained at low relative velocities smaller than 1 km s^{-1} , while values of the MOID are rarely larger than 0.01 au. This suggests that the meteoroid that originated the Motopi Pan meteorite is very likely related to 454100. This result is consistent with what suggested by de la Fuente Marcos & de la Fuente Marcos (2019). The small relative velocities are also compatible with a rotational fission origin, that could be in turn suggested by rotation period estimates obtained from photometry (see Sec. 5). On the other hand, extrapolating a clear separation age from the histogram of t_{\min} is not an easy task. Two concentrations appear between 0 and -5 kyr and at around -30 kyr of evolution, however their statistics is poor. Overall, only a few percent of minima are achieved after roughly 50 kyr of dynamical evolution, and therefore we could only conclude that the separation event most likely happened in the last 50 kyr. A more accurate and thorough dynamical analysis, including also orbital clones for the candidate NEA parent body, would be required to better determine the separation age.

The pair Motopi Pan–2017 MC3 shows a concentration of minima at relative velocity $\Delta V \sim 5 \text{ km s}^{-1}$, happening between -5 and -7.5 kyr. Other concentrations with low MOID values are achieved after 80 kyr of backward dynamical evolution, however they are vastly spread in relative velocity, spanning values of ΔV from $\sim 1.5 \text{ km s}^{-1}$ up to $\sim 5 \text{ km s}^{-1}$. Therefore, while simulations show that the two objects may be somewhat related, the separation event appears to be different from that that originated the pair Motopi Pan–2017 MC3.

Finally, the pair Motopi Pan–2009 FZ4 is qualitatively similar to Creston–2021 JN2. A large concentration of minima of d , gathered around $\Delta V \sim 1 \text{ km s}^{-1}$ and at MOID values smaller than 0.005 au, appears at -10 kyr of dynamical evolution. This also suggest a possible correlation between the two objects, compatible with both a collision event or a rotational fission.

Another plausible hypothesis is that the meteoroid that originated Motopi Pan, 2017 MC3, and 2009 FZ4 all come from 454100, which is the largest asteroid among them, and they all originated during the same event. Additional more accurate numerical simulations would be needed to explore this scenario.

4.14 Arpu Kuilpu–2022 QJ2

Figure 10, seventh row, shows the evolution of the orbital clones of the meteoroid associated to the Arpu Kuilpu meteorite in the planes (R_a, ω) and (R_d, ω) . The evolution of the candidate parent body 2022 QJ2 is depicted by green dots. As in most of the previous

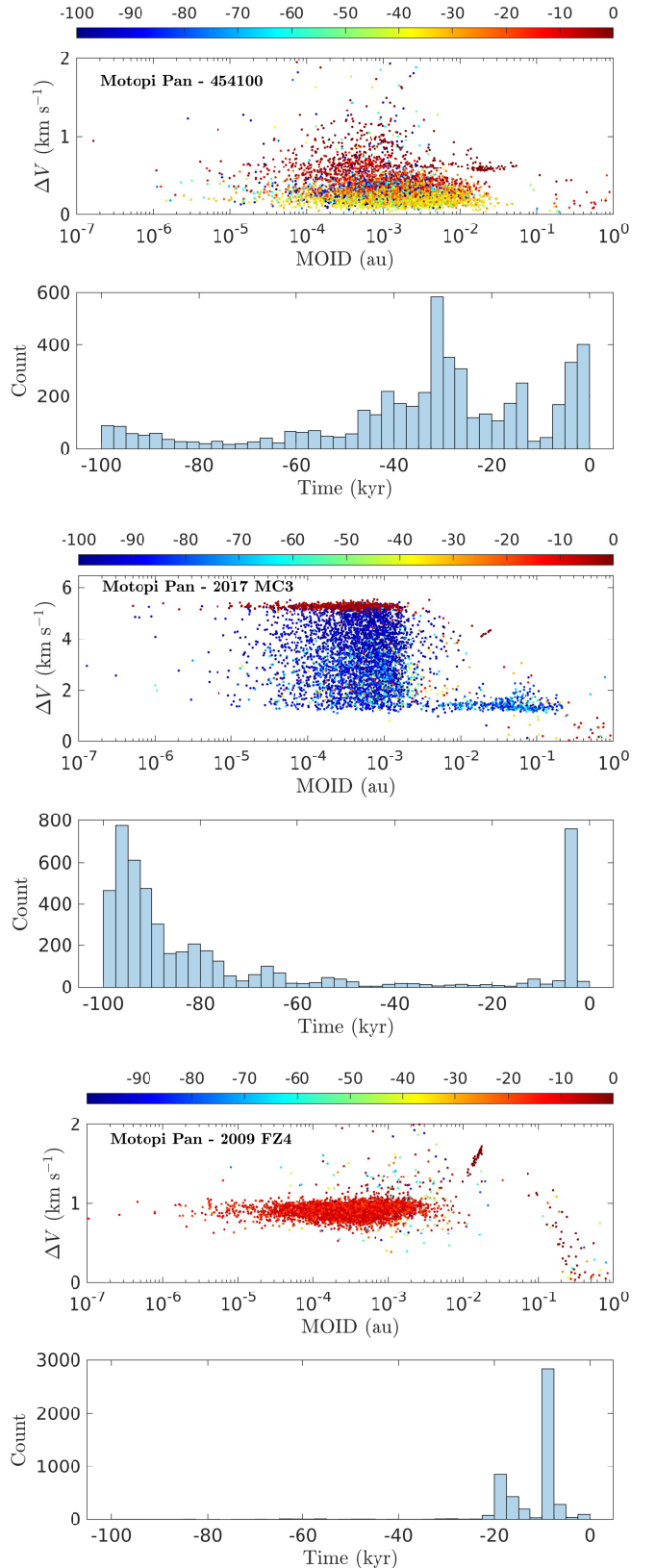


Figure 11. Distributions of MOID vs. relative velocity at the MOID at time t_{\min} , and distribution of t_{\min} , for the pairs Motopi Pan–454100, Motopi Pan–2017 MC3, and Motopi Pan–2009 FZ4.

cases, the two paths are in good agreement. Figure 9 shows the distribution of MOID and ΔV at the minima of d . All the minima are attributed at low relative velocities, however the MOID spans values as low as $\sim 10^{-4}$ au up to ~ 1 au, which seem to be too large to suggest a possible correlation. Note also that these orbits are deeply placed in the 3:1 mean-motion resonance with Jupiter (see e.g. Fenucci, Gronchi & Novaković 2023), and therefore concluding an association based on the properties of the secular evolution is harder, as pointed out above. We consider therefore this association as spurious. In addition, we found that during the backward evolution 1254 meteorite clones were expelled from the Solar System, by effect of deep close encounters with Jupiter. This suggests that the orbit of the meteoroid that originated the Arpu Kuilpu meteorite can be traced back only for a limited amount of time due to chaos produced by close approaches. We found that the expulsion times all happen after 10 kyr of backward dynamical evolution.

5 DISCUSSION

Our results from the previous sections are summarized in Table 4. On a total of 20 possible meteorite–NEA pairs, in 8 cases it was not possible to say whether the association is real or not due to the orbital chaos. In the remaining 12 meteorites cases a physical association appear possible, with a range of minimum speed differences from 0.5 to 6 km s^{-1} : the lowest speed is for the Sutter’s Mill–2016SL2 pair, while the highest is for Križevci–2022RQ. Anyway the characteristic orbital speed difference is about 1 km s^{-1} , a value that appear compatible with an impact event.

The ages of the collisions appear to be on the order of tens of thousands of years, a much lower value than the dynamic life time of a NEA of about 10 Myrs Gladman et al. (1997), therefore the separation must have occurred when the progenitor was already part of the NEAs population. The case of Pribram and Neuschwanstein is peculiar because the age of separation from the asteroid 482488 appear similar, 20–30 kyr, so they were probably born in the same impact event. In Section 4.1 we already noted that, even if the cosmic-ray exposure time of the two meteorites are different (12 Myr Pribram, 48 Myr Neuschwanstein), this does not prevent them from having a common origin. Most likely 482488, considering the diameter, is a rubble pile asteroid as Bennu, made up of blocks with very different and complex exposure histories. Also very interesting is the case of Motopi Pan which appears to be associated with three asteroids, even if the sequence of separation between these bodies is not clear. Also for Motopi Pan the cosmic-ray exposure time is high and estimated to be 19.2 ± 2.4 Myr (Jenniskens et al. 2021). If we suppose that Motopi Pan, 2017 MC3 and 2009 FZ4 were born from the same collision event between an unknown asteroid and 454100 which, being the largest of the three must be considered the main asteroid, then it is likely that the separation age is between -2 kyr and -10 kyr and that there are other small meteoroids on similar orbits that could collide with the Earth in the future. Effectively, according to de la Fuente Marcos & de la Fuente Marcos (2019), it is possible that 2018 LA is associated with 454100 and the χ -Scorpiids meteor shower.

Now the question that needs to be answered is: this typical separation time of tens of thousands of years, is it consistent with impact events? To establish if the typical separation time value found from the orbital analysis of meteorites and NEAs appears reasonable we use a simple collision model to estimate the expected collision frequency for a NEA of about 0.1 km in diameter (the typical size of Table 3) which undergoes a collision with micro-NEAs of the order

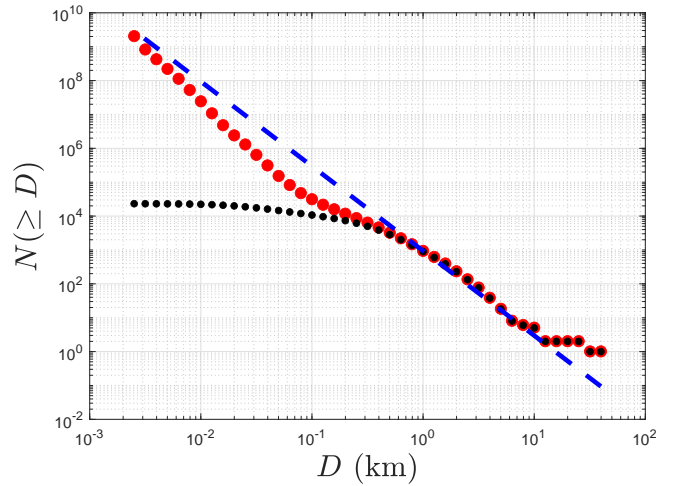


Figure 12. A log-log plot of the NEAs cumulative diameter distribution according to Harris & Chodas (2021) model (red dots) and the observed ones (black dots). The dashed blue line is the simple power law $N(\geq D) = 940 \times D^{-2.5}$. This exponential law is what one would expect in the case of a population of bodies that has undergone a collisional evolution in which the destructive process depends only by the collision speed and the size ratio between the colliding bodies (de Pater & Lissauer 2010). The constant 940 normalizes it to the Harris & Chodas (2021) model for asteroids 1 km in diameter or larger.

of 2 m in diameter. The starting point is the NEAs population model of Harris & Chodas (2021), see Fig. 12 for a plot.

From the cumulative distribution of this model we have $N_1(\geq D_1 = 0.1 \text{ km}) \approx 3.1 \times 10^4$ (type 1 NEAs) and $N_2(\geq D_2 = 0.0025 \text{ km}) \approx 2.05 \times 10^9$ (type 2 NEAs). To estimate the collision frequency of type 1 NEAs immersed in a population of type 2 NEAs, we assume a simple particle-in-a-box model with type 1 NEAs fixed, and type 2 NEAs moving randomly with relative velocity $\Delta V \approx 15 \text{ km s}^{-1}$ within an interaction volume V_{int} (Wetherill 1967; Farinella & Davis 1992):

$$f = \frac{\pi N_1 N_2 (D_1 + D_2)^2 \Delta V}{4V_{\text{int}}}. \quad (12)$$

In Eq. (12) N_1 is the bodies number of the target population, N_2 the bullets population while D_1 and D_2 are their respective diameters. The model represented by Eq. (12) has some limits: there is not a well-defined volume within the NEAs can move, and the relative motion is not completely random as occurs in a gas, however the model can be adequate for estimates of orders of magnitude. A first estimate of the interaction volume for NEAs can be obtained by considering the explosions in the Earth’s atmosphere reported in the CNEOS database⁹.

As of Jan 31, 2023, there are 945 observed explosions in the atmosphere since April 15, 1988. On average, one atmospheric explosion every 13.445 days, with an estimate total impact energies ranging from 0.1 to 100 kt (1 kt = 4.184×10^{12} J), with a median value of about 0.2 kt. Most of these bodies are of asteroidal origin, therefore with typical atmospheric speeds of 10–20 km s^{-1} . If we assume an average value of about 15 km s^{-1} and a bulk density of about 3500 kg m^{-3} , the energy range 0.1–100 kt corresponds to a range of about 1–10 m in diameter, with a median value of about 2 m. As a typical

⁹ <https://cneos.jpl.nasa.gov/fireballs/>

diameter value for this population of very small NEAs we assume this value.

From the estimate number of this population given by [Harris & Chodas \(2021\)](#) and assuming that the observed collision frequency $f \approx 8.61 \times 10^{-7} \text{ s}^{-1}$ was not biased, reversing Eq. (12) we can obtain V_{int} using for D_1 the gravitational diameter of the Earth ($D_1 = 2 \times 7950 = 15\,900 \text{ km}$) with $\Delta V \approx 15 \text{ km s}^{-1}$. Considering that the Earth is only one, in this case $N_1 = 1$. Doing so we find $V_{\text{int}} \sim 7 \times 10^{24} \approx 10^{25} \text{ km}^3$, equivalent to a cube with a side of about 1.4 au.

Now with our estimate of the V_{int} value, we can estimate the collision frequency of the NEAs with $D_1 \geq 0.1 \text{ km}$ ($N_1 \approx 3.1 \times 10^4$) with the whole NEAs population with $D_2 \geq 2 \text{ m}$ ($N_2 \approx 2 \times 10^9$). We found $f \approx 1.1 \times 10^{-12} \text{ s}^{-1}$, so we can expect a collision roughly every 30 000 years. This rough estimate makes it reasonable to find a certain number of meteorite-NEA pairs not older than a few tens of thousands of years.

We made an alternative estimate of V_{int} assuming it is a torus with a square section and using the median values of a , e and i for the population of observed NEAs. The median values of the typical orbit are $a \approx 1.7 \text{ au}$, $e \approx 0.45$ and $i \approx 9^\circ$, so the internal radius of a square section torus is $R_1 = a(1 - e) \approx 0.93 \text{ au}$ while the external one $R_2 = a(1 + e) \approx 2.46 \text{ au}$. The average height of the orbit above ecliptic is $h = (R_2 \sin(i) + R_1 \sin(i))/2 \approx 0.26 \text{ au}$ and the volume of the square section torus is $V_{\text{int}} = 2\pi h(R_2 - R_1)(R_2 + R_1) \approx 10^{25} \text{ km}^3$, in agreement with the previous value estimated from the collision frequency of the micro-NEAs.

Based on these results, it seems reasonable to assume that the very large population of micro-NEAs collide with small NEAs, generating a part of the meteorites found on Earth. Our starting sample consisted of 38 meteorites (Table A1) but only 10 of them appear associated with a known NEA, which means that about $10/38 \sim 25\%$ of the meteorites probably originate directly in the NEAs population, mainly from little collision events in the inner Solar System, rather than from asteroid collisions in the main belt. In summary, the collisions that occur in the main belt can also continue to occur between the NEAs, generating a minority part of the meteorites that we find on Earth.

In order to better characterize the possible connection from meteorites and NEAs, we invite the astronomers to observe at least the candidate parent objects with the lowest orbital uncertainty by taking advantage of the next favorable close encounter. Unfortunately most of the Table 4 asteroids have very uncertain orbits and need to be recovered. Furthermore, given the small size, in general large telescopes are needed. The best candidates for observation are 2014K F22, which will be 0.02 au from Earth on May 25, 2025 with a magnitude of +21, and 454100 which will be 0.084 au on May 30, 2035. This latter NEA is quite large and will reach maximum brightness on May 20, with visual magnitude +17.2: photometric and spectroscopic observations could be carried out to determine both the rotation period and the spectral type of this very intriguing asteroid. Finally, it is important to point out two features of the method used here. The first one is that the dynamics of objects in the NEA region is naturally subjected to chaos, with Lyapunov times often not larger than few tens of thousands years, and the method is expected to identify pairs with an age comparable to this timespan. Older pairs may be found only in really stable cases for which the Lyapunov time is much longer, but they would be very rare, considering also that the orbits of meteorites cross the orbit of the Earth by definition.

The second remark is that the association between meteorites and NEAs is naturally subjected to changes. While about 96% of NEAs of 1 km in diameter are known, estimates suggest that only about 44% of NEAs smaller than 140 m and the 5% of NEAs smaller than 50

Table 4. List of the candidate pairs meteorites-NEA with the possible separation age, minimum MOID and minimum ΔV . Note that for all the meteorites with high orbital inclinations Pribram, Neuschwanstein, Bunburra, Jesenice and Annama it was possible to establish a separation event. I=Inconclusive results, S=spurious association.

Meteorite Name	NEA	Age (kyr)	MOID (au)	ΔV (km s ⁻¹)
Pribram	482488	-30/-25	$10^{-4} - 10^{-3}$	1
Peekskill	2014 KF22	-2.5	$10^{-4} - 10^{-2}$	0.8
Neuschwan.	482488	-25/-20	$10^{-4} - 10^{-3}$	1
Park Forest	2021 WT	S	-	-
Bunburra Rockhole	2021 FB	S	-	-
Jesenice	2017 FZ64	-10 or -17	$10^{-5} - 10^{-2}$	1
Košice	2021 NV5	I	-	-
	2019 ST2	I	-	-
Križevci	2022 RQ	-7.5	$10^{-6} - 10^{-3}$	6
	2013 BR15	S	-	-
Sutter's Mill	2016 SL2	-2.5	$10^{-4} - 10^{-1}$	0.5
Annama	2016 RX	-2.5 or -35	$10^{-3} - 10^{-1}$	4 or 3
Žd'ár nad S.	2005 VE7	I	-	-
Creston	2021 JN2	-7.5/5	$10^{-5} - 10^{-2}$	3.5
Hamburg	2022 UF	-10/0	$10^{-4} - 10^{-1}$	1
	2021 PZ1	S	-	-
Motopi Pan	454100	-2.5/-30	$10^{-5} - 10^{-2}$	< 0.5
	2017 MC3	-5	$10^{-5} - 10^{-2}$	5
	2009 FZ4	-10	$10^{-6} - 10^{-2}$	1
Arpu Kuilpu	2022 QJ2	S	-	-

m have been discovered ([Harris & Chodas 2021](#)). Table 3 shows that asteroids as small as 10–20 m can still be dynamically associated to meteorites, thus more and more progenitor candidates can be found as the number of known NEAs increases. It is therefore important to attempt better dynamical associations as the catalogue of NEAs increases and their orbits improve in quality.

6 CONCLUSIONS

The aim of our work was try to determine possible parents NEAs for meteorites. We considered 38 meteorites whose heliocentric orbit was determined by triangulating their fireball during the fall and of which the coordinates of the true geocentric radiant and speed (which is not the entry speed into the atmosphere) are available. Starting from the encounter conditions of the Earth with the meteorites and the known NEAs population, DN criterion based on geocentric quantities was computed with a certain limit threshold, finding 20 possible NEA–meteorite pairs.

The orbital evolution of these 20 pairs was studied starting from the time of the fall and going back in time. To account for the greater uncertainty of meteorite orbital elements with respect to NEAs, a population of 5000 clones was used for each meteorite. For 12 of these potential pairs, concentrations of distance minima were found in the phase space formed by the MOID of the orbits and by the relative speed at MOID. The minimum MOID between the orbits is around 10^{-4} au , while the relative velocity is about 1 km s^{-1} , with time scales of the order of tens of thousands of years for the NEA-meteorite separation time. The relative speed of about 1 km s^{-1} suggests that collisions events separated the meteorite from the parent NEA. Other events that could generate separation, such as rotational instability, tidal destruction or thermal fracturing, would result in much lower relative speeds. Very interesting and unique are the Pribram and Neuschwanstein meteorites which, despite the diver-

sity in cosmic-ray exposure time, probably separated from the same NEA with a rubble pile structure, (482488) 2012 SW20, about 20–30 kyr ago. The Motopi Pan meteorite is also very interesting, having three possible candidate NEA parent bodies: 454100, 2017 MC3, and 2009 FZ4. The NEA 454100 as progenitor of Motopi Pan was also found independently by [de la Fuente Marcos & de la Fuente Marcos \(2019\)](#).

Based on a simple NEA-in-the-box model, it is reasonable to expect times of the order of a ten thousand years between collisions of NEAs of the order of 100 m in diameter and much smaller NEAs of the order of 2 m in diameter, in good agreement with what we found. So it seems reasonable to say that a part of the recovered meteorites, about 25% of the starting meteorite sample according to our estimates, does not originate from collisions in the main belt, but from collisions events that occur directly in the population of small and very small NEAs in the inner Solar System. For this reason it is important to physically characterize the small asteroids probably associated with meteorites, even if they are objects which, even during close passages with the Earth, require large instruments to be observed. The possible meteorite-NEA pairs are also indicators of potential meteoroid showers whose radiants – if exist – should be close to those of the meteorites. This work of matching between the radiants of meteorites and the radiants of already known meteor showers will be the subject of a forthcoming paper.

ACKNOWLEDGEMENTS

The authors want to thank very much Giovanni Valsecchi (INAF-Institute of Space Astrophysics and Planetology), for the comments and suggestions that made the paper much better than the original. Many thanks to SpaceDyS and Fabrizio Bernardi for the use of the OrbFit code for NEAs-Earth encounter conditions computation. Finally our thanks go to the referee, whose suggestions make this paper much better than original.

DATA AVAILABILITY

The data underlying this article will be shared on reasonable request to the corresponding author.

REFERENCES

Avdellidou C. et al., 2022, *A&A*, 665, L9
 Babadzhanyan P. B., Williams I. P., Kokhirova G. I., 2012, *Mont. Not. R. Astron. Soc.*, 420, 2546
 Binzel R. P., Xu S., 1993, *Science*, 260, 5105
 Bland P. A., Spurný P., Towner M. C., Bevan A. W. R., Singleton A. T., Bottke W. F., Greenwood R. C., et al., 2009, *Sci*, 325, 1525.
 Borovička, J., Spurný, P., 2008, *A&A*, 485, L1-L4
 Borovička, J., et al., 2013, *Meteoritics & Planetary Science* 48, 1757
 Bottke W. F., Nolan M. C., Greenberg R., 1993, *LPSC*, 24, 159
 Bottke W. F., Morbidelli A., Jedicke R., Petit J.-M., Levison H. F., Michel P., Metcalfe T. S., 2002, *Icar*, 156, 399
 Bottke W. F., Vokrouhlický D., Rubincam D. P., Nesvorný D., 2006, *AREPS*, 34, 157
 Bottke W. F., Vokrouhlický D., Walsh K. J., Delbo M., Michel P., Lauretta D. S., Campins H., et al., 2015, *Icar*, 247, 191
 Carbognani A., 2017, *Planet. Space Sci.*, 147, 1
 Carry B., 2012, *Planetary and Space Science*, 73, 98
 Chambers J. E., Migliorini F., 1997, *DPS*
 de la Fuente Marcos C., de la Fuente Marcos R., 2019, *A&A*, 621, A137

Delbo M., Libourel G., Wilkerson J., Murdoch N., Michel P., Ramesh K. T., Ganino C., et al., 2014, *Nature*, 508, 233
 Del Vigna A., Faggioli L., Milani A., Spoto F., Farnocchia D., Carry B., 2018, *A&A*, 617, A61
 de Pater I., Lissauer J. L., 2010, *Planetary Sciences*, second edition, Cambridge University Press.
 Drumond J. D., 1981, *Icarus*, 45, 545
 Eugster O., 2003, *Geochemistry*, 63, 3
 Farinella P., Davis D. R., 1992, *Icarus*, 97, 111
 Fenucci M., Gronchi G. F., Saillenfest M., 2022, *CeMDA*, 134, 23
 Fenucci M., Novaković B., 2022, *SerAJ*, 204, 51
 Fenucci M., Gronchi G. F., Novaković B., 2023, *A&A*, 672, A39.
 Ferrari F., Raducan S. D., Soldini S., Jutzi M., 2022, *The Planetary Science Journal*, 3, 177
 Folkner W. M., Williams J. G., Boggs D. H., Park R. S., Kuchynka P., 2014, *IPNPR*, 42-196, 1
 Flynn G. J., Consolmagno G. J., Brown P., Macke R. J., 2018, *Chemie der Erde*, 78, 269
 Gaffey M. J., Gilbert S. L., 1998, *Meteoritics and Planetary Science*, 33-6, 1281
 Gladman J. B., et al., 1997, *Science*, 277, 197
 Granvik M., Morbidelli A., Jedicke R., Bolin B., Bottke W. F., Beshore E., Vokrouhlický D., et al., 2016, *Natur*, 530, 303
 Granvik M., Morbidelli A., Vokrouhlický D., Bottke W. F., Nesvorný D., Jedicke R., 2017, *A&A*, 598, A52
 Granvik M., Morbidelli A., Jedicke R., Bolin B., Bottke W. F., Beshore E., Vokrouhlický D., et al., 2018, *Icar*, 312, 181
 Granvik M., Brown P., 2018, *Icar*, 311, 271
 Gronchi G. F., Milani A., 2001, *Icarus*, 152, 58
 Gronchi G. F., Michel P. 2001, *Icarus*, 152, 48
 Harris A. W., Chodas P. W., 2021, *Icarus*, 365, 114452
 Jenniskens P., 2008, *Icarus*, 194, 13
 Jenniskens P. et al., 2019, *Meteoritics and Planetary Science*, 54-4, 699
 Jenniskens P. et al., 2021, *Meteoritics and Planetary Science*, 56-4, 844
 Jewitt D., 2012, *The Astronomical Journal*, 143, 66
 Jopek T. J., 1993, *Icarus*, 106, 603
 Jopek T. J., Valsecchi G. B., Froeschlé Cl., 1999, *Mont. Not. R. Astron. Soc.*, 304, 751
 Kyrilenko I., Krugly Yu. N., Golubov O., 2021, *Astronomy & Astrophysics*, 655, A14
 O’Leary B., 1977, *Science*, 197, 363
 Melikyan R. E. et al., 2021, *JGR: Planets*, 126-9, 1
 Morbidelli A. et al., 1994, *A&A*, 282, 955
 Moskovitz N. A., Fatka P., Farnocchia D., Devogèle M., Polishook D., Thomas C. A., Mommert M., et al., 2019, *Icar*, 333, 165
 Peña-Asensio E., Trigo-Rodríguez J. M., Rimola A., 2022, *AJ*, 164, 76
 Pravec P., Harris A. W., 2000, *Icar*, 148, 12
 Pravec P. et al., 2006, *Icar*, 181, 63
 Pravec P. et al., 2010, *Nature*, 466, 1085
 Quan-Zhi Ye, 2018, *Planetary and Space Science*, 164, 7
 Revelle D. O., Brown P. G., Spurný P., 2004, *Meteoritics & Planetary Science*, 39, 1605
 Rožek A., Breiter S., Jopek T. J., 2011, *Mont. Not. R. Astron. Soc.*, 412, 987
 Rubincam D. P., 2000, *Icar*, 148, 2
 Scheeres D. J., 2018, *Icarus*, 304, 183
 Schunová E., Jedicke R., Walsh K. J., Granvik M., Wainscoat R. J., Haghhighipour N., 2014, *Icarus* 238, 156
 Sergeyev A. V., Carry B., 2021, *A&A*, 652, A59
 Southworth R. B., Hawkins G. S., 1963, *Smithsonian Contributions to Astrophysics*, 7, 261
 Spoto F., Milani A., Knežević Z., 2015, *Icar*, 257, 275
 Spurný P., Oberst J., Heinlein D., 2003, *Nature*, 423, 151
 Stoer J., Bulirsch R., 2002, *Introduction to Numerical Analysis*, 3rd edn., Texts in Applied Mathematics 12
 Valsecchi G. B., Jopek T. J., Froeschlé Cl., 1999, *Mont. Not. R. Astron. Soc.*, 304, 743
 Vernazza P. et al., 2015, *The Formation and Evolution of Ordinary Chondrite*

- Parent Bodies in Asteroid IV (Edited by Michel P., DeMeo F. E. and Bottke W. F.)
Vernazza P. et al., 2008, *Nature*, 454, 858
Warner, B. D., Harris, A. W., Pravec, P., 2009, *Icarus* 202, 134-146. Updated 2023 April 24. <http://www.MinorPlanet.info/php/lcdb.php>
Wetherill G. W., 1967, *JGR*, 72, 2429. doi:10.1029/JZ072i009p02429
Whipple F. L., 1983, *IAU Circ. No.* 3881
Williams I. P., Wu Z., 1993, *Mont. Not. R. Astron. Soc.*, 262, 231
Zhang Y., Michel P., 2020, *A&A* 640, A102

APPENDIX A: ADDITIONAL TABLES AND FIGURES

This paper has been typeset from a $\text{\TeX}/\text{\LaTeX}$ file prepared by the author.

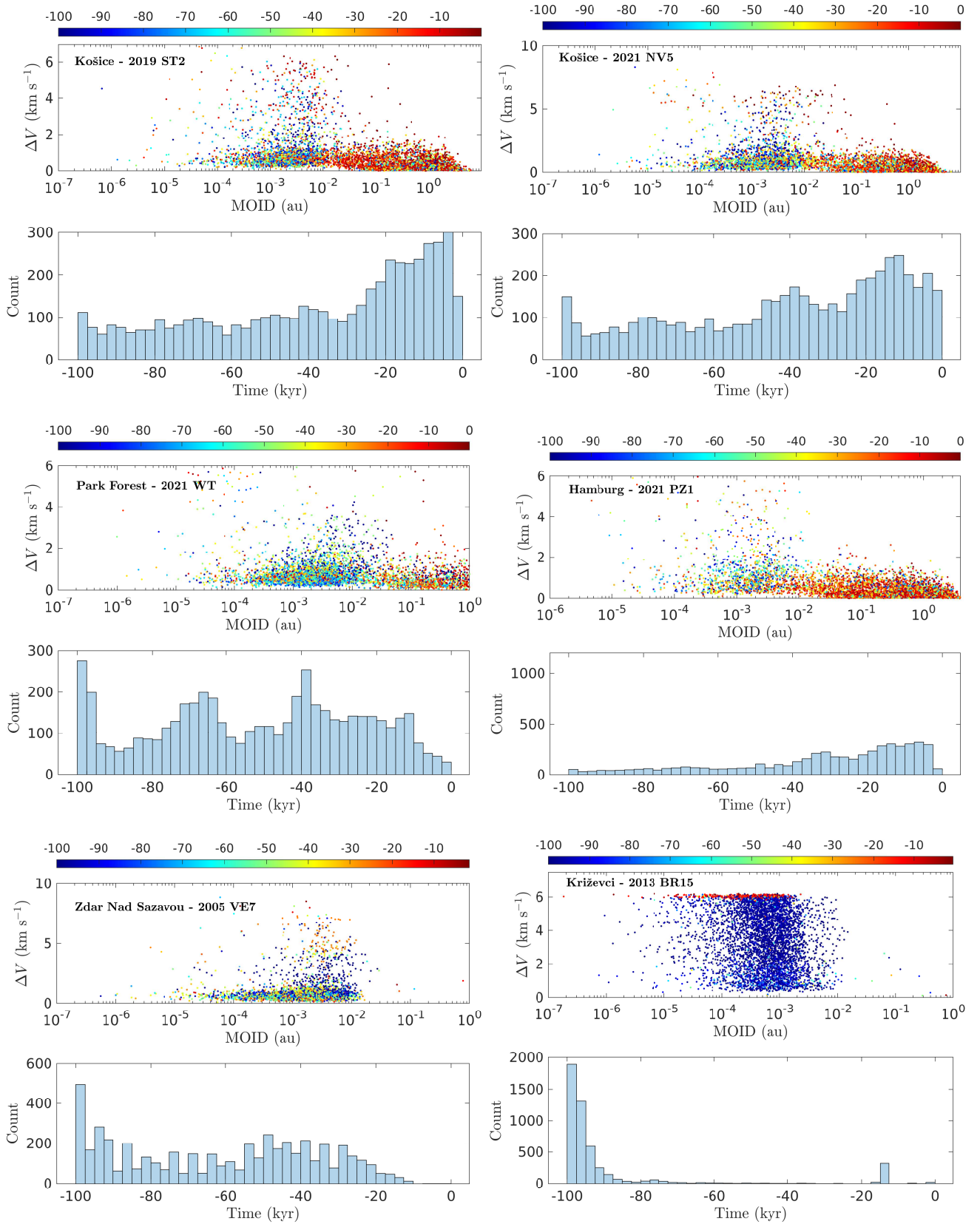


Figure A1. Distributions of the relative velocity vs. the MOID at the time t_{\min} and distribution of t_{\min} , for the pairs Košice–2021 VN5, Košice–2019 ST2, Park Forest–2021 WT, Hamburg–2021 PZ1, Žďar nad Sázavou–2005 VE7, and Křiževci–2013 BR15.

Table A1. Meteorites list with Earth encounter conditions U , θ , ϕ and λ from true radian and geocentric velocity used to compute the distance D_N with the NEAs whose orbit intersects Earth's orbit. Earth's encounter condition type: DePre = descending node before perihelion; DePost = descending node post perihelion; AsPost = ascending node post perihelion; AsPre = ascending node before perihelion.

N	Name	Type	U_x	U_y	U_z	U	θ (°)	ϕ (°)	λ (°)
01	Pribram	DePre	-0.530	0.136	-0.209	0.585	76.602	248.500	197.827
02	Lost City	DePost	0.182	0.223	-0.380	0.477	62.088	154.399	104.486
03	Innisfree	DePost	0.013	0.272	-0.391	0.477	55.223	178.072	138.216
04	Benesov	DePre	-0.330	0.119	-0.487	0.601	78.549	214.129	227.004
05	Peekskill	AsPost	0.305	0.114	0.095	0.339	70.326	72.648	16.836
06	Moravka	DePre	-0.170	0.016	-0.636	0.658	88.619	194.936	226.304
07	Neuschwanstein	DePre	-0.527	0.128	-0.227	0.588	77.454	246.648	196.832
08	Park Forest	DePre	-0.511	0.164	-0.066	0.541	72.314	262.609	185.867
09	Villalbeto de la Peña	DePost	0.513	0.243	-0.000	0.567	64.643	90.016	103.615
10	Bunburra Rockhole	AsPost	0.140	-0.113	0.137	0.226	119.987	45.620	297.597
11	Maribo	DePre	-0.850	-0.072	0.012	0.853	94.827	270.821	117.693
12	Jesenice	DePre	-0.082	0.177	-0.199	0.279	50.485	202.461	199.232
13	Grimsbj	DePost	0.163	0.077	-0.573	0.601	82.641	164.141	2.953
14	Košice	DePre	-0.226	0.258	-0.044	0.346	41.726	258.936	160.085
15	Križevci	DePre	-0.481	0.061	-0.012	0.485	82.767	268.572	135.641
16	Sutter's Mill	DePost	0.868	-0.089	-0.038	0.873	95.831	92.528	212.704
17	Novato	AsPost	0.110	0.223	0.119	0.276	35.992	42.966	24.954
18	Chelyabinsk	DePost	0.494	0.073	-0.095	0.508	81.697	100.845	146.425
19	Annama	DePre	-0.675	0.011	-0.255	0.722	89.111	249.320	208.600
20	Žd'ár nad Sázavou	DePre	-0.618	0.062	-0.053	0.623	84.283	265.137	77.304
21	Porangaba	DePost	0.317	0.210	-0.185	0.423	60.210	120.304	108.927
22	Sarıççek	DePre	0.000	0.058	-0.436	0.440	82.466	179.943	339.830
23	Creston	AsPre	-0.369	0.026	0.076	0.378	86.026	281.624	30.282
24	Murrili	AsPost	0.055	0.261	0.074	0.277	19.531	36.839	64.641
25	Ejby	DePre	-0.167	0.269	-0.022	0.317	32.014	262.643	137.289
26	Dishchii' bikoh	DePost	0.178	-0.031	-0.371	0.413	94.267	154.373	252.112
27	Dingle Dell	DePre	-0.270	0.210	-0.086	0.353	53.409	252.276	38.271
28	Hamburg	DePre	-0.282	0.244	-0.013	0.373	49.169	267.298	116.614
29	Motopi Pan	DePre	-0.404	0.055	-0.078	0.415	82.425	259.072	251.853
30	Ozerki	DePre	-0.086	-0.151	-0.289	0.337	116.565	196.552	269.400
31	Arpu Kuilpu	AsPre	-0.383	0.224	0.043	0.446	59.794	276.379	250.376
32	Flensburg	AsPost	0.482	0.188	0.141	0.536	69.445	73.659	349.212
33	Cavezzo	DePost	0.006	0.199	-0.084	0.216	22.960	175.900	100.523
34	Novo Mesto	DePost	0.618	-0.056	-0.147	0.638	95.027	103.368	158.978
35	Madura Cave	DePre	-0.277	-0.108	-0.002	0.297	111.220	269.609	268.703
36	Traspena	DePre	-0.398	-0.025	-0.079	0.407	93.518	258.751	117.833
37	Winchcombe	AsPost	0.056	0.267	0.010	0.273	12.045	79.694	160.241
38	Antonin	DePre	-0.212	-0.057	-0.417	0.471	96.894	206.993	292.575

Table A2. Nominal orbits of the 19 candidate NEAs progenitors at epoch 2460000.5 JD.

Designation	a (au)	e	i ($^{\circ}$)	Ω ($^{\circ}$)	ω ($^{\circ}$)	M ($^{\circ}$)
2016 RX	2.564762534806265	0.7430159649322464	13.32038927171481	163.6869477168528	92.94244137657836	219.1642830492932
2016 SL2	2.062474771961578	0.7694417719511251	1.81036115435297	17.57269810440301	90.90339137084725	343.6082890477512
2021 FB	0.8427246777483847	0.2545728694223879	9.748690090403196	358.4518153292897	28.7554149600137	315.2583299127406
2022 UF	2.5730036883023004	0.63341114989874336	0.36753632746543397	218.37443715719363	131.38839048745186	37.406284232043475
2021 PZ1	2.364634799369776	0.6005267765114393	0.3837223115640573	312.3287880862847	43.02588027657282	145.221744238352
2021 NV5	2.4232937397214642	0.60395245231432071	1.7146217533748498	286.87427481414164	37.913588036324398	147.52756370586465
2019 ST2	2.360713484135783	0.5936746616690849	0.9134261986212852	148.3443111992481	260.5757535991638	350.1867624028299
2022 RQ	1.4635773482255161	0.49759911285260583	1.4321781313495281	281.20578540149700	148.86736375858436	62.584884321126040
2013 BR15	1.554708606396463	0.5204835798046532	1.95477797282755	102.901345532338	284.8925546883462	32.86431971445231
482488	2.4599816749788479	0.67863969498218224	10.164746072164734	209.59680478373903	62.360038457242275	270.76914909176315
2014 KF22	1.4975257070308479	0.42062292021733566	4.9474665864368523	68.058161464574212	237.29322439428816	253.92446624875143
2021 JN2	1.173687000118325	0.3328521597176412	2.569641121995291	90.88855796610243	33.76881352655698	210.6776283527358
2017 FZ64	1.93653518628377	0.4973485243004753	7.654708065751632	163.3336464620337	52.71333823686388	60.912511625351
2021 WT	2.388580875809223	0.6740508905169703	3.450236129095224	60.66733234698395	298.9417278570344	132.9039422465572
2005 VE7	2.3322473963386656	0.71721231566531540	7.5150458469052781	287.12863098453755	14.946913926937720	330.01202768332274
454100	1.3314136872194222	0.418262476165029	4.543665801377	24.781742651553	298.166430154473	331.192762486796
2017 MC3	1.1384900776606286	0.655699554855858	7.073023632531	111.187680237372	300.270880329344	183.467292685508
2009 FZ4	1.1218473724744065	0.249500520614930	4.200036083824	357.105648161701	288.875765616387	178.952261478393
2022 QJ2	2.6048219825436361	0.654500985555764	1.610888877536	289.421112283214	342.207267115725	54.547932515782